Microstructural development via synergic application of Binder jJetting and Quenching and Partitioning (QP) on commercial AISI 4340

Belfi, M.; Mariani, M.; Martin Saint-Laurence, P.M.; Santofimia, M.; Gruttadauria, A.; Deirmina, F.; Lecis, N.; Barella, S.

DOI
10.1016/j.matchar.2025.114839

Publication date
2025

Document Version
Final published version

Published in
Materials Characterization

Materials Characterization 222 (2025) 114839

Contents lists available at ScienceDirect

Materials Characterization

journal homepage: www.elsevier.com/locate/matchar

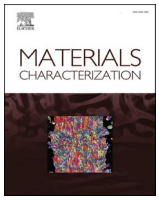

Microstructural development via synergic application of Binder Jetting and Quenching and Partitioning (QP) on commercial AISI 4340

M. Belfi [a,*], M. Mariani [a,*], P. Martin [b], M. Santofimia [b], A. Gruttadauria [a], F. Deirmina [c], N. Lecis [a], S. Barella [a]

[a] Department of Mechanical Engineering, Politecnico di Milano, 20156 Milano, Italy
[b] Department of Materials Science and Engineering, TU Delft, 2628 CD Delft, the Netherlands
[c] Sandvik Additive Manufacturing, Sandvik Machining Solutions AB, Sandviken, Sweden

ARTICLE INFO

Keywords:
AISI 4340 steel
Binder jetting
Quenching and partitioning
Decarburization
Microstructural development

ABSTRACT

This study investigates the microstructural development of commercial low-alloyed AISI 4340 steel through the synergistic application of Binder Jetting and Quenching and Partitioning (QP) processes. The material in the as-sintered condition exhibited significant variations in microstructure and mechanical properties, primarily influenced by the processing route. Carbon content was influenced by the building technique as decarburization was observed at different intensities mainly during the heating stage of sintering, driven by carbothermic reduction. Vacuum-debinding was found to be optimal, leading to the most homogeneous microstructure, predominantly granular bainite with superior hardness and tensile strength. Different QP treatments were optimized considering the decarburization effect on the optimal as-sintered condition, stabilizing 4–8 % retained austenite in a martensitic matrix, with optimal results observed after isothermal holding at either 220 °C or 240 °C for 30 min. These conditions resulted in high UTS values of 1231 MPa and 1151 MPa, respectively, compared to 750 MPa in the as-sintered state. Despite high tensile properties, A% was limited by the presence of residual porosity. This study highlights the critical importance of controlled debinding and sintering atmospheres as well as decarburization-informed QP treatments in achieving desirable microstructural and mechanical properties in additively manufactured AISI 4340 steel components.

1. Introduction

In the last decade, binder jetting (BJT) has emerged as a suitable additive manufacturing process, viable to produce complex metallic and ceramic parts. BJT involves the precise layer-by-layer deposition of a liquid binding agent onto a powder bed allowing the creation of three-dimensional objects. These are thermally treated in a manner comparable to typical powder metallurgy processes: they are debinded to remove the organic binding agent and then sintered to achieve the requested density. Recent progresses in binder formulations, printhead technologies, and post-processing methodologies have propelled the advancement of BJT, thereby amplifying its appeal for industrial-scale production [1].

By integrating BJT with thermal treatments, manufacturers can precisely control the microstructural evolution of metallic components, leading to tailored material properties that are optimized for specific functional requirements. An example of this is the production of high-strength steels (HSS), such as the medium carbon AISI 4340, which

Abbreviations: α', Martensitic ferrite; α_B, Bainitic ferrite; AS, As-sintered; BCC, Body-centered cubic; BJT, Binder jetting; CCE, Constrained carbon equilibrium; δ_F, Delta ferrite; E, Young Modulus; EBSD, Electron backscatter diffraction; EDX, Energy dispersive X-ray spectroscopy; ε_{max}, Elongation at failure; FCC, Face-Centred cubic; FE-SEM, Field emission-scanning Electron microscope; FM, Fresh Martensite; GB, Granular Bainite; HAGB, High angle grain boundary; HSS, High strength steel; HV, Vickers hardness; ICP-OES, Inductively coupled plasma-optical emission spectroscopy; IPF, Inverse pole figure; LAGB, Low angle grain boundary; LOM, Light optical microscope; KAM, Kernel average Misorientation; MA, Martensite/austenite; MEX, Material extrusion; MIM, Metal injection molding; PAG, Prior austenitic grain; PAGB, Prior austenitic grain boundary; PEG, Polyethylene glycol; QP, Quenching and partitioning; QT, Quenching and tempering; RA, Retained austenite; SLPS, Supersolidus liquid phase sintering; SSS, Solid state sintering; T_{aust}, Austenitization temperature; T_p, Partitioning temperature; t_p, Partitioning time; T_q, Quenching temperature; UTS, Ultimate tensile strength; XRD, X-ray diffraction; YS, Yield strength.

* Corresponding authors.
E-mail addresses: marco.belfi@polimi.it (M. Belfi), marco.mariani@polimi.it (M. Mariani).

https://doi.org/10.1016/j.matchar.2025.114839
Received 26 November 2024; Received in revised form 4 February 2025; Accepted 9 February 2025
Available online 13 February 2025

has remarkable strength, toughness, and wear resistance, combined with the possibility of controlling the hardness and ductility by post-processing, which is potentially useful in a variety of applications [2–5]. Indeed, 4340 steels can be modified through Quenching and Tempering (QT) processes so that the microstructure can be manipulated to maximize mechanical strength while maintaining good ductility [6–8]. Alternatively, Quenching and Partitioning (QP) treatment has the potential to enhance steel performance leading to a novel combination of ultra-high strength and improved toughness and ductility [9,10]. QP is a heat treatment first proposed by Speer et al. [11] which consists of full austenitization above the critical temperature A_3 and a quenching step between the martensite start (M_s) and martensite finish (M_f), followed by isothermal holding called partitioning, and a final quench down to room temperature. The partitioning step is meant to activate carbon diffusion from the supersaturated martensitic matrix to austenite, thereby stabilizing the carbon-enriched austenite [12,13]. The final step is a second quenching to room temperature. The presence of a hard martensitic matrix imparts a high tensile strength to the material, whereas retained austenite (RA) provides ductility. When subjected to external loads, austenite transforms into martensite through strain-induced transformation. In this way, not only the amount but also the stability of RA significantly influences the final properties of the material. The strain-induced transformation occurs from less stable to more stable austenite grains, contributing to the high tensile properties and improved ductility [14–16].

Following the previous, the QP process parameters, such as the quenching temperature (T_q), partitioning temperature (T_p), and partitioning time (t_p) should be tailored to enhance the fraction and stability of RA, avoiding competitive phenomena and undesired phase transformations. T_q should be sufficiently high to guarantee a consistent fraction of untransformed austenite, but sufficiently low to provide an adequate fraction of martensite able to partition sufficient carbon to austenite and stabilize it at room temperature [17,18]. Excessively high T_p and t_p may generate conditions for isothermal bainite formation [19,20], which decreases the amount of austenite and has lower strength with respect to martensite. If T_p and t_p are too low, insufficient carbon enrichment of the austenite is obtained, and part the non-stabilized austenite can further transform during the second quenching phase into non-tempered fresh martensite (FM). This phase should be avoided due to its brittleness [18]. Moreover, the formation of transition carbides during the partitioning step can reduce the concentration of free carbon available for austenite stabilization, and thus, should be limited as well. Although the precipitation of transition carbides remains uncontrolled, cementite formation is usually suppressed in QP steels through silicon addition at concentrations higher than 1 wt% [21,22] which also aids austenite stabilization [23]. However, commercial steels typically feature a lower silicon content owing to production issues, leading to the inability to avoid completely carbide formation, thus reducing the effectiveness of the QP treatment. Nevertheless, different studies have shown that QP can also be applied to low-Si commercial steels with good results in terms of the RA fraction and final tensile properties, opening up the possibility of effective application of this treatment to a wider range of high-strength steels. [18,24–26]

Given the strict correlation between microstructural and mechanical properties, tight control of the initial phase composition is necessary to design optimal QP treatments. Indeed, as-sintered steels obtained by BJT or similar techniques (e.g., metal injection molding (– MIM) and material extrusion (– MEX) [27–29]) might present a series of features that are not common in their as-cast counterparts, thus affecting the outcome of thermal treatments: inclusions (e.g., oxides/carbides) generated by the presence of organic residues, large residual porosity with anisotropic distribution, δ ferrite formed at high sintering temperatures, and coarse grains. It is fundamental to investigate the microstructural development throughout the manufacturing process to achieve tighter control of the as-sintered components and to facilitate and maximize the effectiveness of sequent thermal treatments. Indeed, most steels, especially non-stainless classes, cannot be employed in the as-produced condition and their required performance is granted only by post-processing.

Currently, a limited number of studies have dealt with non-stainless steels [30–32], specifically AISI 4340 alloy for BJT. Among these, the focus is mainly on the optimization of the sintering conditions to maximize the final density and minimize geometrical distortions by combining supersolidus liquid-phase sintering (SLPS) and solid state sintering (SSS), with a proposed description of the oxide reduction role in the presence of hydrogen [33–35]. Similarly, Rayner et al. observed the degassing behavior of 5120 steel particles for BJT in reducing and inert atmospheres and concluded that CO production was the most relevant mechanism between debinding and sintering temperatures [36]. Therefore, it is suggested that the interaction between oxygen and carbon both from the atmosphere and the material might interfere with the densification of the printed components. The role of carbon residue might also lead to additional carbides formation, which seems to be significantly detrimental in the case of SLPS owing to their alignment along the grain boundaries, which can lead to premature failure at small elongations [37]. Given the criticality of the construction technique, it is necessary to apply a post-processing heat treatment to ensure adequate mechanical properties.

Quenching and partitioning couples high mechanical properties with improved ductility, consequently it may be particularly attractive to make up for the limited tensile properties given by the BJT building technique, especially in the case of non-total densification. Achieving limited decarburization and high densification in the as-sintered condition is essential for obtaining a starting material compatible with QP treatment; consequently, the building technique was analyzed in depth to find an optimized as-sintered condition for further treatments. The present study aims to determine the effect of consecutive steps, from printing to sintering, particularly the debinding cycle, on the final microstructure of a AISI 4340 steel. The role of surface oxide formation on the particles and their carbon-induced thermal reduction at high temperatures in an inert atmosphere is assessed. The development of phases and inclusions is described and correlated with the specific processing conditions to identify an optimal route for the production of 4340 components suitable for QP treatments. These treatments were designed and optimized considering the decarburization given by the sintering step and were performed on the BJT samples produced with the optimized cycle. The goal is to achieve a BJT-built AISI 4340 with a tailored microstructure and a set of tensile properties that are improved with respect to the as-sintered condition.

2. Materials and methods

2.1. Samples production

The feedstock material is an AISI 4340 steel produced by gas atomization by Sandvik Osprey®. The carbon content of 0.43 wt% corresponds to the upper boundary of the standard composition (C = 0.37–0.43 wt%). The particle size distribution has a reported D_{90} of 16 μm, which is typical of MIM-grade feedstocks [27]. The actual composition was measured using inductively coupled plasma optical emission spectroscopy (ICP-OES) and LECO analysis according to ISO/IEC 17025:2017, and the particle size distribution was obtained using the laser diffraction method: the values are provided in Table 1. CALPHAD simulations were performed using Thermo-Calc 2023a software (TCFE12: Steel/Fe-Alloys v12.0 database) using the chemical composition reported in Table 1, to predict the equilibrium phase fractions at different temperatures and to design an appropriate sintering profile and sequent heat treatments [38]. To account for possible variations in the characteristic temperatures owing to instability in the chemical composition during processing, simulations were performed with higher and lower carbon contents in the range of 0.03 wt% to 0.63 wt%. The results are shown in Fig. 1.

The components were printed using an ExOne Innovent + machine

Table 1
Chemical composition and size distribution of the particles.

Chemical composition [wt%]									Size distribution [μm]		
Ni	Cr	Mn	C	Mo	Si	P	S	Fe	D10	D50	D90
1.8	0.8	0.7	0.43	0.3	0.25	0.009	0.006	Bal.	3.5	7.5	14.0

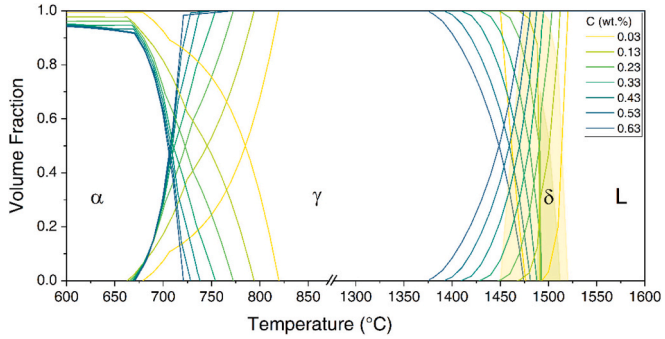

Fig. 1. Volumetric fractions of main phases (α, γ, and liquid fraction variations are marked by straight lines for all compositions, δ is highlighted by the colored areas for C = 0.03/0.13 %) at varying temperatures obtained by Thermo-Calc simulation.

with a layer thickness of 50 μm and a binder saturation of 55 %. The ligand was a commercial aqueous-based solution (AquaFuse®) containing polyethylene glycol (PEG) precursors. Curing was performed in a static air furnace at 180 °C for 6 h to consolidate the polymer within the green bodies. Debinding was performed at 470 °C for 1 h in three different atmospheres: air, fluxed argon with residual oxygen, or low vacuum (10^{-2} mbar). Afterwards, sintering was performed under argon at different peak temperatures for 3 h at a heating rate of 200 °C h^{-1} followed by furnace cooling. A summary of these cycles is presented in Table 2. From the prediction reported in Fig. 1 for the theoretical composition (C = 0.43 wt%), δ phase is not thermodynamically stable within the sintering temperature range, thus it should be avoided in any case, whereas SLPS aided by a relevant liquid fraction should be expected only at sintering temperatures above 1450 °C.

2.2. Heat treatments

The study of thermal post-processing conditions (i.e., QP thermal treatments) was performed on a selected set of specimens that proved to be the most reliable in terms of chemistry (i.e., C content), microstructural and mechanical properties, as well as low geometrical distortions upon sintering. A Bähr 805 A/D dilatometer was used to thermally treat such specimens and to identify the phase transformations occurring during the applied heat treatments. Cylindrical specimens (Ø4 mm × 10 mm) were tested. All specimens were inductively heated under dynamic vacuum of 10^{-4} mbar and quenched under a protective atmosphere of continuously flushed helium gas. An S-type thermocouple was spotwelded on the surface of each specimen to control and monitor the temperature. The studied QP treatments are shown in Fig. 2. Heat treatments were designed based on the chemical composition and the critical temperatures obtained in the optimal as-sintered state, as described later. The austenitization temperature (T_{aust}) was set to 850 °C (70 °C higher than A_3). The Constrained Carbon Equilibrium (CCE) was applied to compute T_p, taking into account the 85–15 rule proposed by Celada-Casero et al. [17] to optimize the effectiveness of the treatment regarding microstructural development and final properties. In addition, a sample (Q) was quenched to room temperature. Cooling rates (25 °C s^{-1}) were chosen to avoid phase transformations during quenching.

2.3. Materials characterization

Digital caliper measurements and Archimedes' method were employed to evaluate sintering linear shrinkage (Δx, Δy and Δz along the three main axes) and density variations, respectively. Five samples were analyzed for each condition to ensure sufficient repeatability.

The material was ground, polished, and etched with Nital 2 % reagent. The microstructure was studied using a Nikon Eclipse LV150NL light optical microscope (LOM) and a Zeiss Sigma 500VP field-emission scanning electron microscope (FE-SEM) combined with energy-dispersive X-ray spectroscopy (EDX) and electron backscatter

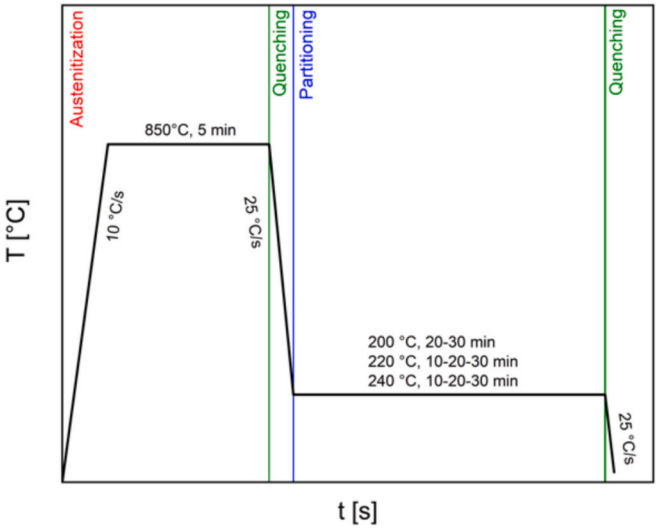

Fig. 2. Schematic summary of QP heat treatments.

Table 2
Debinding and sintering conditions. The samples name reports the thermal treatments variables: the debinding atmosphere (a – air, A – Argon, V – vacuum) and the maximum sintering temperature.

Sample	Debinding			Sintering		
	Temperature [°C]	Time [h]	Atmosphere	Temperature [°C]	Time [h]	Atmosphere
a1475	470	1	Air	1475	3	Ar
A1425	470	1	Ar	1425	3	Ar
A1440	470	1	Ar	1440	3	Ar
A1475	470	1	Ar	1475	3	Ar
V1440	470	1	Vacuum	1440	3	Ar
V1475	470	1	Vacuum	1475	3	Ar
V1510	470	1	Vacuum	1440 + 1510	3	Ar

diffraction (EBSD). The latter measurements were obtained with a 20 kV/12 kV accelerating voltage and a 0.5/0.1 μm step size at 1000×/5000× magnification, respectively. EBSD data were post-processed using HKL CHANNEL5 software (Tango module): Kernel average misorientation (KAM) maps were elaborated with a 3 × 3 filter size and misorientation grain angle of 5°, and high angle grain boundaries (HAGBs) were detected by setting the minimal misorientation angle at 10°. Phase identification on sintered components was performed by means of X-Ray Diffraction (XRD) using a Rigaku Smartlab SE diffractometer, with a Cu-Kα source in the range of 30–100° with a step size of 0.02° and a scanning speed of 1° min^{-1}. The phase analysis of the QP specimens was performed by XRD using a Bruker D8 Advance diffractometer with Bragg-Brentano geometry equipped with a graphite monochromator and Vantec position-sensitive detector, using Co-Kα radiation in the 30–130° range, a step size of 0.035°, and a counting time per step of 1 s. A V6 Divergence slit was employed, as well as a scatter screen of 8 mm. The voltage and current were set at 40 kV and 40 mA, respectively. No spinning was imposed. MAUD software was employed to perform Rietveld refinement analysis [39]. This was conducted by considering a pseudo-Voigt function, Popa rules size-strain model, Popa LB line broadening model, no planar defects, and *E*-WIMW texture model for the profile fittings. Additionally, Lanthanum Hexaboride Powder LaB6_660c standard reference material (a = 0.4156826 ± 0.000008 nm) was utilized to determine instrumental broadening and instrumental offset. Two figures of merit (σ and Rwp) were used as indications for adequate refinement, considering upper values of 2 and 10 pct., respectively. The austenite lattice parameter a_γ is correlated to the carbon content through a modified version of the Dyson-Holmes equation presented in [40] and reported in Eq. 1.

$$a_\gamma = 3.556 + 0.0453X_c + 0.00095X_{Mn} + 0.0056X_{Al} \quad (1)$$

where X_C, X_{Mn}, and X_{Al} correspond to the content of carbon, manganese, and aluminum (in wt%), respectively.

The carbon content after both debinding and sintering was measured using combustion analysis with a LECO CS744 machine for three samples per specimen.

Vickers microhardness (HV) was measured with a load of 300 gf and dwell time of 15 s in multiple areas of all samples in both the central and surface regions. Tensile tests were performed on 4 mm thick "dogbone" specimens compliant to the "Standard Flat Unmachined Tension Test Specimens for Powder Metallurgy (P/M) Products" described in ASTM E8/E8M, obtained after debinding in vacuum and sintering in argon at a strain rate of 2 mm min^{-1} on selected samples before and after thermal treatments.

3. Results

3.1. Sintered components

3.1.1. Microstructural characterization

The sintered samples exhibited comparable densification and shrinkage rates (Fig. 3). Considering a theoretical density of 7.80 g cm^{-3}, the achieved relative density values were limited to below 92 % in most cases, except for a1475 and V1510 specimens. Typical linear shrinkage rates of binder-jetted components are within the 14–18 % range in the planar directions (X and Y axes) and slightly above 20 % in the building direction (Z axis) [41]. V1510 displays significantly different shrinkages owing to the consistent shape distortions that occurred during sintering, which suggests the formation of an excessive fraction of liquid phase as could be expected from the simulation in Fig. 1. In the cases of the V1440 and V1470 specimens, Δz is lower with respect to other samples owing to irregularities on the bottom surface of the components, generated by the known "bleeding" defects that may occur in the BJT.

The carbon contents reported in Fig. 4 reveal that significant

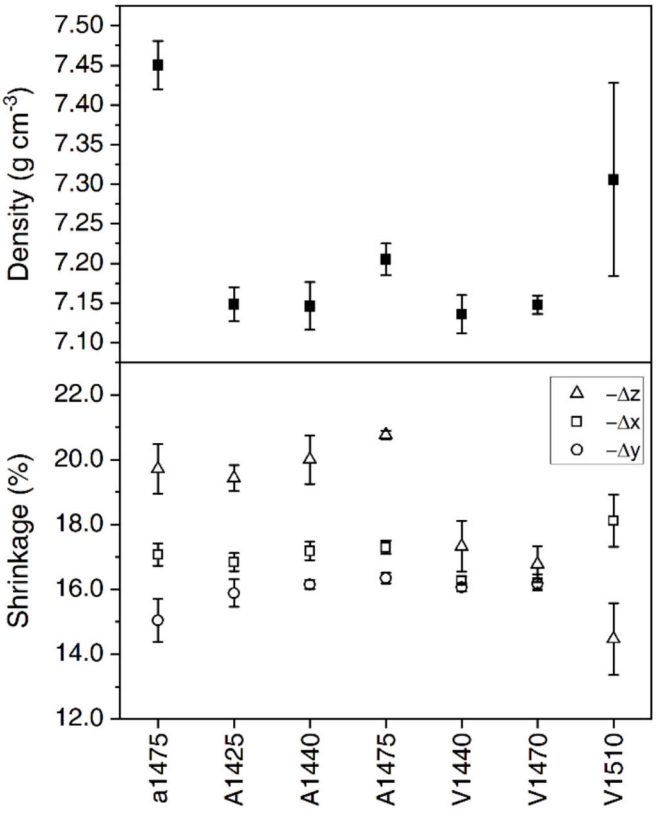

Fig. 3. Density and linear shrinkage values of the as-sintered samples.

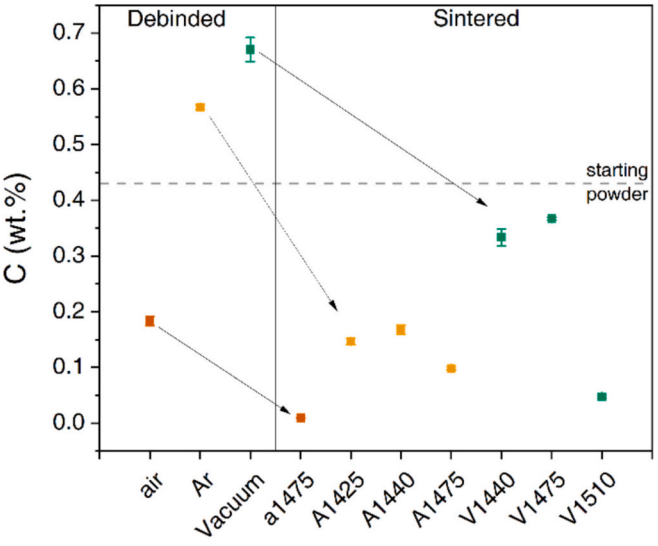

Fig. 4. Carbon content of debinded and sintered specimens.

variations occurred during the processing, leading to different outcomes depending on the debinding atmosphere and sintering temperature [42,43]. Indeed, it can be observed that debinding in an inert environment (Ar or vacuum) leads to carbon enrichment owing to incomplete burnout of the organic ligand, as observed in previous studies [44,45]. In contrast, air-debinding promoted decarburization despite the treatment temperature was relatively low (470 °C).

In all cases, early final-stage densification was achieved; thus, the residual porosity was almost completely closed, spherical, and preferentially aligned along the interlayer interfaces, as shown in the LOM pictures of a1475 and V1510 specimens (Fig. 5). The micrographs

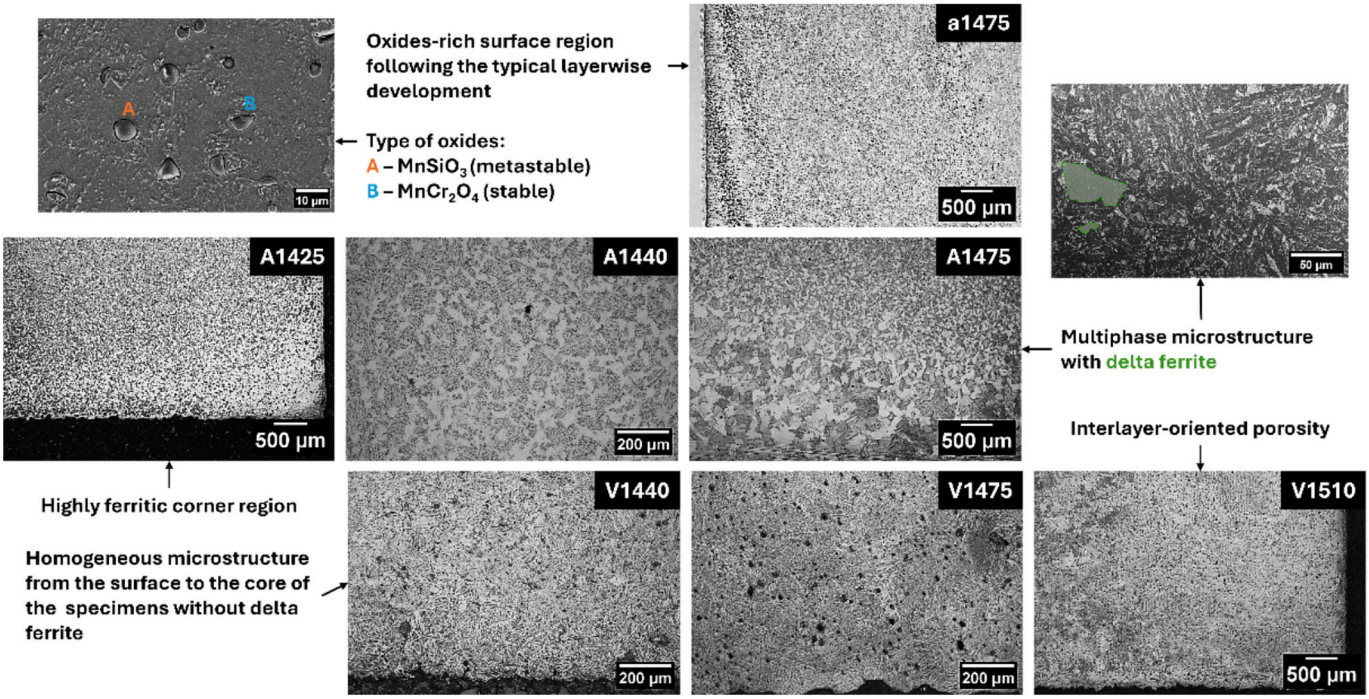

Fig. 5. Metallographies of the sintered specimens.

obtained by LOM also revealed different types of microstructures as a function of the three different studied debinding atmospheres. The air-debinded sample (a1475) features a two-phase microstructure with δ ferrite (δ_F, light grey) and bainite (dark grey). In addition, it can be observed that most of the black spots do not correspond to closed pores but rather to spherical oxides, whose concentration is evident in the surface region. EDX analyses (Fig. 6) revealed three main classes for these inclusions:

- Mn- and Si-rich oxides likely correspond to rhodonite with an olivine structure ($MnSiO_3$).
- Mn-, Cr-, and Fe-rich oxides in minor quantities are spinel oxides obtained by the transformation of metastable rhodonite at high temperatures [46].
- SiO_2, which is a residue from polishing operations.

Ar-debinded specimens, however, presented only a limited number of oxide inclusions but still exhibited a biphasic microstructure. Additionally, the phase distribution is not homogeneous throughout the sample: ΔF is predominant and enlarged in close proximity to the surface and corners of the samples (see specimens A1425 and A1475).

Finally, the vacuum-debinded parts presented a homogeneous microstructure characterized by bainitic grains from the core to the surface of the samples in the case of V1440 and V1475, whereas V1510 features a complex microstructure (see Fig. 7).

In Fig. 7, EBSD analyses conducted in the central regions of vacuum- and Ar-debinded samples reveal microstructures characterized mostly by granular bainite (GB), typical of continuous-cooling transformations that, in this case, occurred during the in-furnace cooling after sintering [47]. Prior austenitic grain boundaries (PAGBs) can be identified in grain boundary maps obtained by setting a minimum misorientation angle filter of 10°, knowing that most of the PAGBS should present misorientation values within the 21.1–47.1° range [48]. In the low-magnification images for both V1440 and A1440, the original FCC γ-phase PAGs with a hexagonal morphology can be detected, although HAGBs can also be found within the parent phase. The shape of the PAGs revealed that the sintering process proceeded until the minimization of the surface free energy associated with the grain boundaries and coalescence was promoted, leading to PAGs sizes of several tens of micrometers. The HAGBs found within the parent phase are associated with the boundaries between different packets of the bainitic ferrite (α_B) regions. Such packets feature either an irregular or an elongated form, thus revealing that in some cases, the microstructure tends to develop similarly to upper bainite that should form at lower temperatures with respect to GB, as proposed by Qiao et al. [49]; when the temperature is low enough, diffusion is insufficient to promote the formation of equiaxed regions.

The V1440 high-magnification images revealed the presence of large carbon-rich areas (indicated by the green arrows in Fig. 7) that tend to have a disordered microstructure and display austenitic grains that underwent an incomplete transformation. Owing to the negligible amount of FCC phase, these could correspond either to martensite/austenite (MA) regions or degenerate pearlitic colonies, which are typically found in GB subjected to slow cooling rates ($< 20\ ^\circ C\ min^{-1}$) [50–52]. The low signal of the band-contrast image (dark pixels) and the high signal of the KAM map (bright pixels) seem to confirm this identification. Smaller areas (identified by yellow arrows), especially those at the triple grain junction, feature similar properties; thus, they likely correspond as well to α' obtained by a complete transformation of the austenite, as suggested by the absence of face-centered cubic (FCC) structures.

The equiaxed region in A1440 (indicated by purple arrows) with a low KAM signal corresponds to δ ferrite retained at the core of the Ar-debinded sample.

EBSD and XRD analyses (Fig. 8) confirmed the presence of retained austenite (RA) in all the samples, particularly within the α_B and MA regions. The inverse pole figure (IPF) signal of the FCC phase in the high-magnification image of V1440 confirms that each γ region retains the original crystallographic orientation of the corresponding PAG; the IPF color within the same PAG is identical, whether RA is within α_B or MA.

Because of the uncontrolled cooling rate within the furnace after sintering, the microstructural development of the as-sintered components was not strictly controlled. This promoted the formation of a variety of minor structures that could be neglected for the final properties of the bulk components but might be relevant in the development of automated microstructure recognition systems, as proposed in various

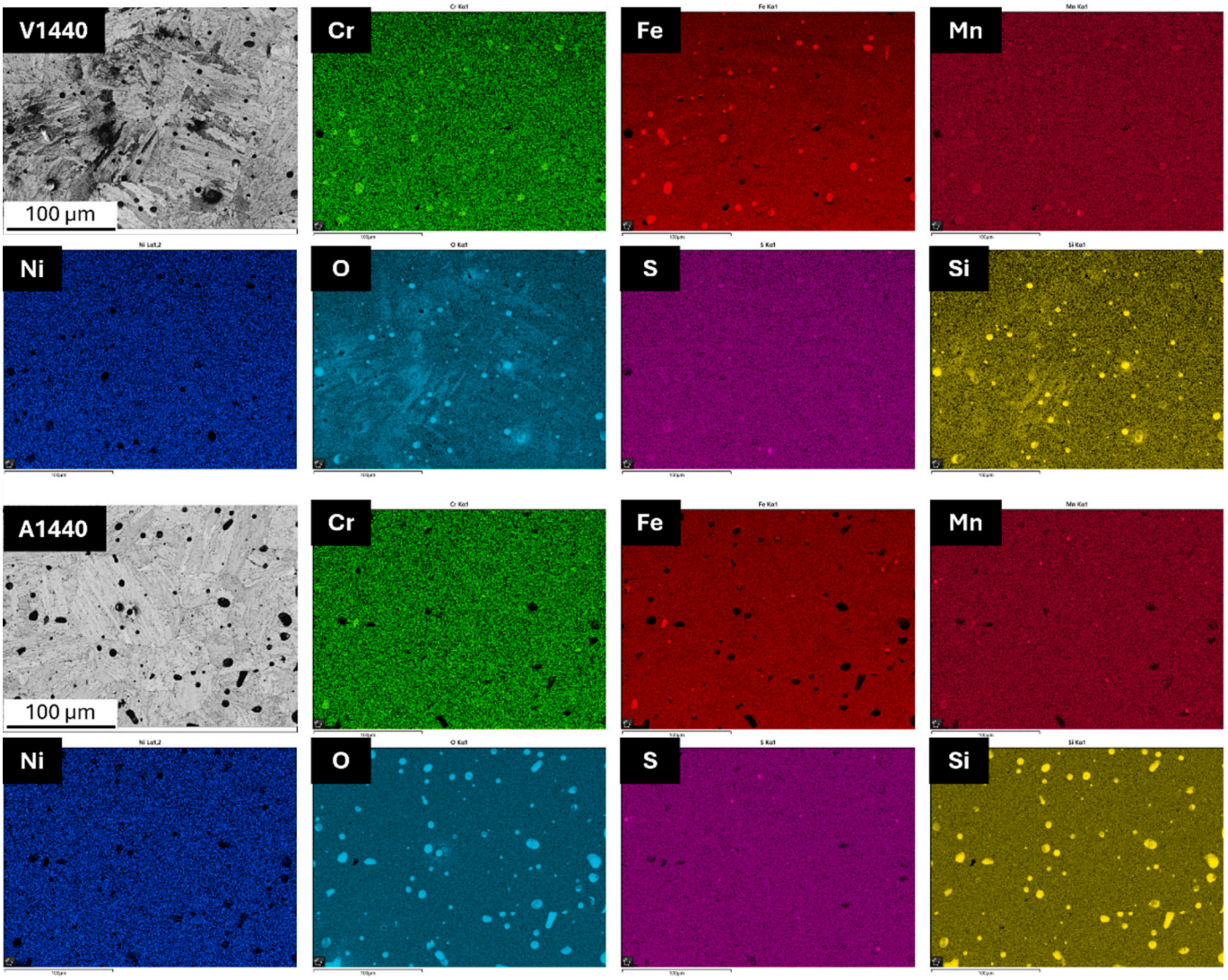

Fig. 6. EDX maps of the V1440 and A1440 specimens.

studies [50,51,53,54]. The SEM pictures in Fig. 9 reveal a series of such structures within the GB, as described above for α'.

At approximately 800 °C, ferrite (α) begins to nucleate and grow in γ. The area in the yellow ellipse along the PAGB features a flat side and curved profile growing within the PAG, which is typical of grain boundary allotriomorphs. The plates within the green areas show oriented growth starting from the PAGBs; thus, they can be identified as primary Widmanstätten ferrite. The area highlighted in light blue shows a series of parallel α_B laths delimited by discontinuous boundaries. These could correspond to short MA grains/films [49–51] forming in a unit of degenerate pearlite obtained from an untransformed area of the PAG that is still not mutated in the GB [53].

3.1.2. Mechanical properties

The microhardness values of the different specimens reflect the variety of microstructures described above. Table 3 shows $HV_{0.3}$ values spanning an extensive range, from approximately 100 to 275. The highest hardness was measured for the V1440 and V1475 specimens, whereas the V1550 and the other two series feature values below 200 HV. It should be noted that the standard deviations are comparable in all cases except for a1475. Samples with extreme loss in carbon, show lower hardness and the samples with C contents in the range of ~0.4 show hardness levels equal to that of annealed 4340 steel (i.e., ~250 HV) [55].

The tensile properties obtained from the vacuum-debinded samples (see Fig. 10) were similar for the V1440 and V1475 specimens, while those of the V1510 experienced a reduction in the yield strength (YS) and ultimate tensile strength (UTS). By contrast, the elongation at break tripled. The reduction in the bainitic fraction is responsible for the lower yield strength, while the limited number of pores avoids the anticipated failure experienced in the other samples.

The V1475 specimen featured both a slightly higher hardness and tensile strength than the V1440 sample, although the phase composition and homogeneity were comparable. This may probably stem from the higher C content of the former.

3.1.3. Suitability for quenching and partitioning treatment

As a result of optimizing the different parameters of the BJT, it was observed that the V1440 case obtained high densification and a carbon content in the sintered condition (0.34 %) that allows the application of QP treatment. Indeed, air- and Ar-debinded conditions contained an extremely limited carbon available to partition, thus irrelevant variations of microstructure and mechanical properties upon the application of QP thermal treatments would be expected. In addition, the relevant presence of δ_F in the surface and, in some cases, in the core regions limit the tailoring of the mechanical properties because these areas would not reach full austenitization above A_3. Consequently, the V1440 condition was the only one chosen for the sequent application of QP heat

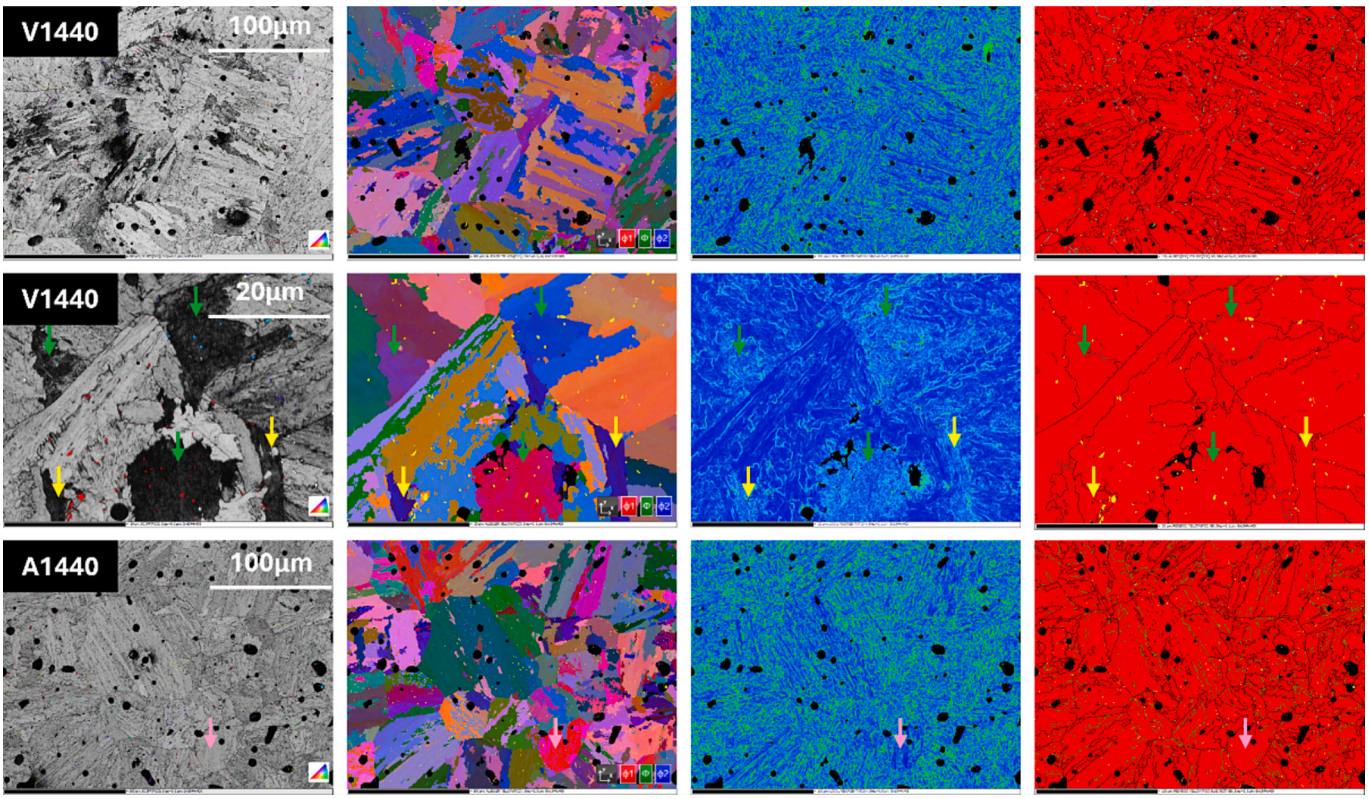

Fig. 7. EBSD analysis of the sintered specimen V1440 (at low and high magnification) and A1440 (at low magnification) with band contrast with IPF signal of the FCC phase, Euler angle with the FCC phase in yellow, KAM and grain boundaries with the FCC phase in yellow maps. (For interpretation of the references to color in this figure legend, the reader is referred to the web version of this article.)

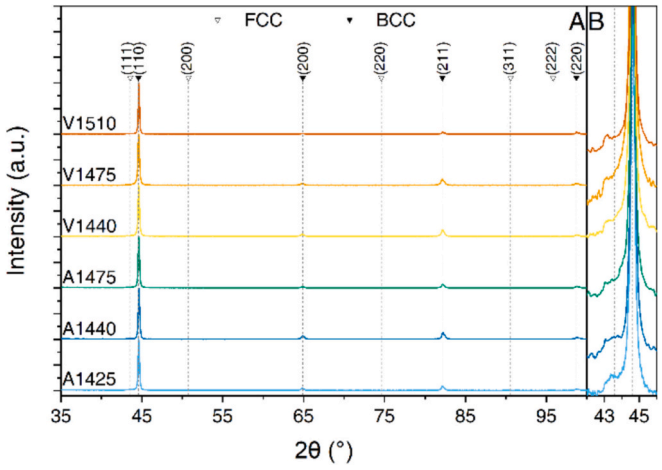

Fig. 8. X-ray diffraction of sintered specimens after debinding in inert atmosphere: A) full spectrum, B) main peaks.

treatments. Hereafter, V1440 will be referred to as the as-sintered (AS) condition, and heat treatments will be exclusively applied to it.

The observed variation in the chemical composition due to decarburization was considered in the design of the QP heat treatments. First, the austenitization temperature was selected to yield fully austenitic matrix, hence 850 °C was selected for a carbon concentration of 0.34 wt % according to the Thermo-Calc simulation shown in Fig. 11A, which implies 70 °C above the calculated A_3. As it was shown in Fig. 2, after austenitization for 5 min, the samples were quenched to 200–220-240 °C (within the M_S – M_{99} window as indicated by the simulation of Fig. 11B) at a cooling rate of 25 °C s^{-1} and maintained for isothermal treatment of 10–20-30 min to promote carbon partitioning from the martensite to the austenite, aiming the stabilization of the austenite at room temperature. Finally, the specimens were quenched in water.

3.2. Heat treatments

XRD was employed to investigate the presence of RA in the QP-treated specimens. The XRD patterns are presented in Fig. 12.

The quantified RA fractions, and carbon concentration in RA, are presented in Fig. 13 as a function of partitioning time.

As can be seen from Fig. 13, the quenched sample presented a small fraction of RA (2 %); meanwhile, the proposed heat treatments conducted to RA values ranging between 4 and 8 %. The highest RA fraction was detected in the 220–30 sample. Although the differences between samples were minimal, some trends were observed. The higher the T_p, the higher the carbon content in austenite, and thus, its mechanical stability. In fact, not only the amount but also stability of RA is reported to influence the final properties of the material [56–58]. As carbon diffusion is favored by a higher t_p, isoT samples partitioned for 30 min showed the highest lattice parameters. Similarly, between the isot conditions, samples partitioned at the highest temperature (240 °C) showed the highest carbon concentration and lattice parameter (3.588 Å). The as-quenched sample showed the lowest a_γ (3.584 Å), indicating a lower carbon content in RA and possibly poor mechanical stability, thus showing the effectiveness of the partitioning step.

Dilatometry was employed to investigate the microstructural evolution during the QP heat treatments. Deviations from the linearity in the dilatation during the thermal cycles are correlated with the microstructural variations occurring in the material. Critical temperatures A_1, A_3 and M_s were thus identified as 746 °C, 778 °C, and 341 °C, respectively, with ±5 °C uncertainty. A_3 and M_s correlate well with the critical temperatures predicted by CALPHAD simulation, presented in Fig. 11,

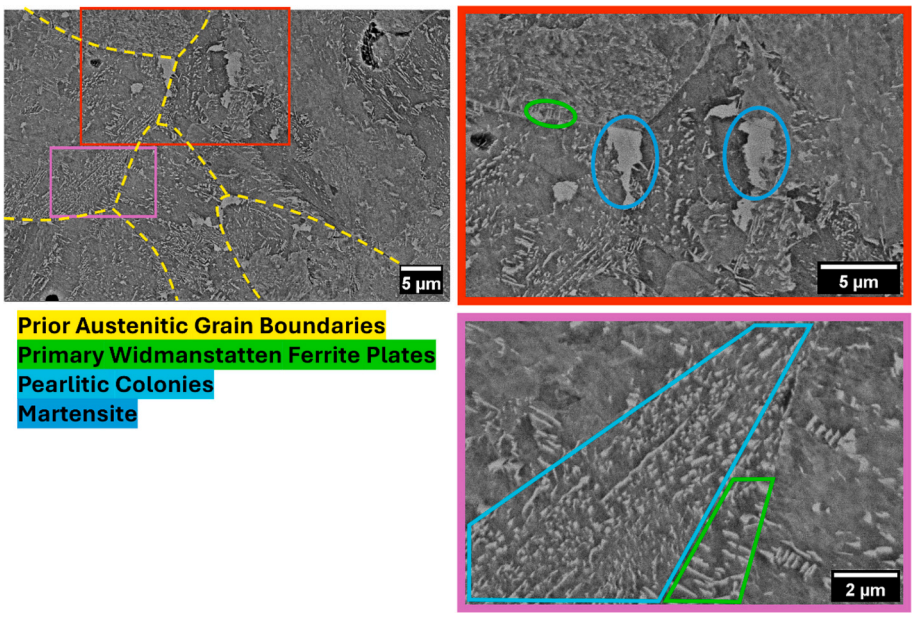

Fig. 9. SEM images at different magnifications of the sintered specimen V1440.

Table 3
Microhardness and tensile properties of the sintered specimens.

Sample	$HV_{0.3}$	E [GPa]	YS [MPa]	UTS [MPa]	ε_{max} [%]
a1475	106 ± 3	–	–	–	–
A1425	158 ± 21	–	–	–	–
A1440	182 ± 12	–	–	–	–
A1475	175 ± 16	–	–	–	–
V1440	234 ± 27	161	544	750	6.0
V1475	275 ± 13	184	611	797	5.0
V1510	142 ± 15	182	229	363	15.5

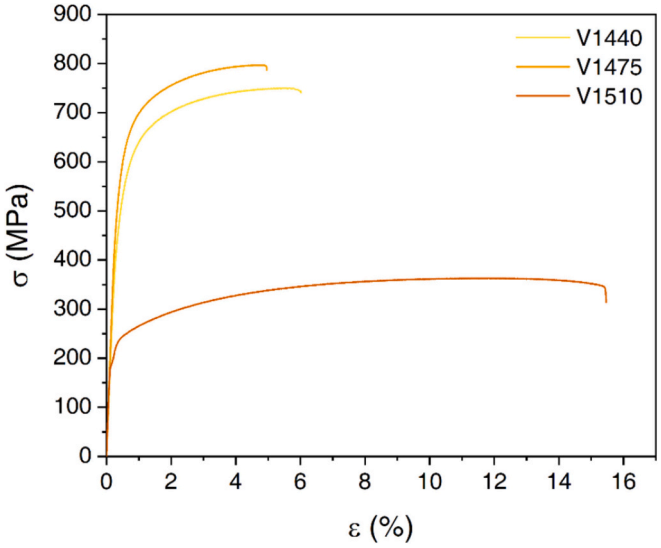

Fig. 10. Tensile test curves of sintered specimens after debinding in vacuum.

especially if the actual chemical composition of the sintered samples is considered, thus confirming the reliability of the modelled features with the correct carbon concentration. No variations in the slope were reported between T_{aust} and M_s, indicating that phase transformations were avoided during quenching, leading to the targeted martensitic – austenitic microstructure at the beginning of the partitioning stage

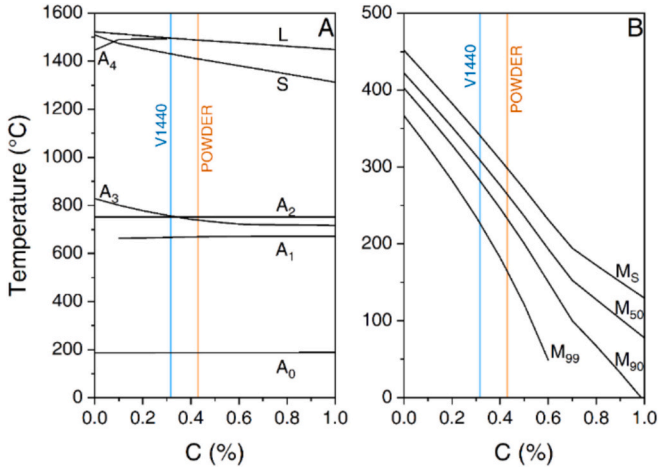

Fig. 11. Thermo-Calc calculation of A) the quasi-binary phase diagram Fe—C for an alloy containing 0.7 Mn, 0.25 Si, (complete); and B) the martensite start temperature M_s and corresponding M_{50}, M_{90} and M_{99} as a function of carbon content for the same alloy content considered in (A).

(Fig. 14).

The overall procedure for the quantification of the phase fraction evolution during quenching is based on the work of Mola et al. [18], represented in Fig. 15, and resumed below:

– $\Delta L/L_0$ was computed at 25 °C for the reference as-quenched (Q) sample.
– Imposing the RA% obtained through XRD, the upper limit of the lever rule (A') was computed, corresponding to an extrapolated 100 % α' condition.

$$\frac{\overline{A'C'}}{\overline{A'B'}} = 0.02$$

– The slope of the interpolation curve for the 100 % α' condition was corrected as follows:

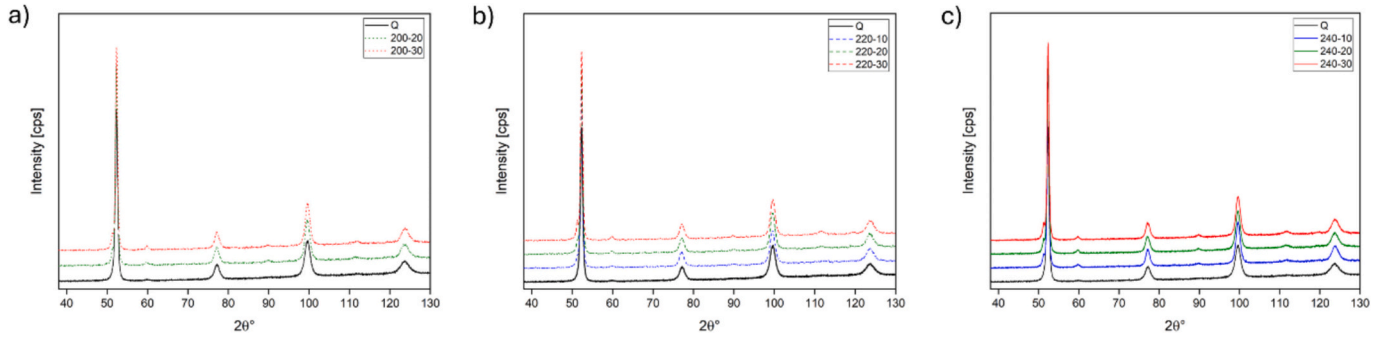

Fig. 12. XRD patterns of the samples treated at different partitioning temperatures: a) 200 °C, b) 220 °C, c) 240 °C.

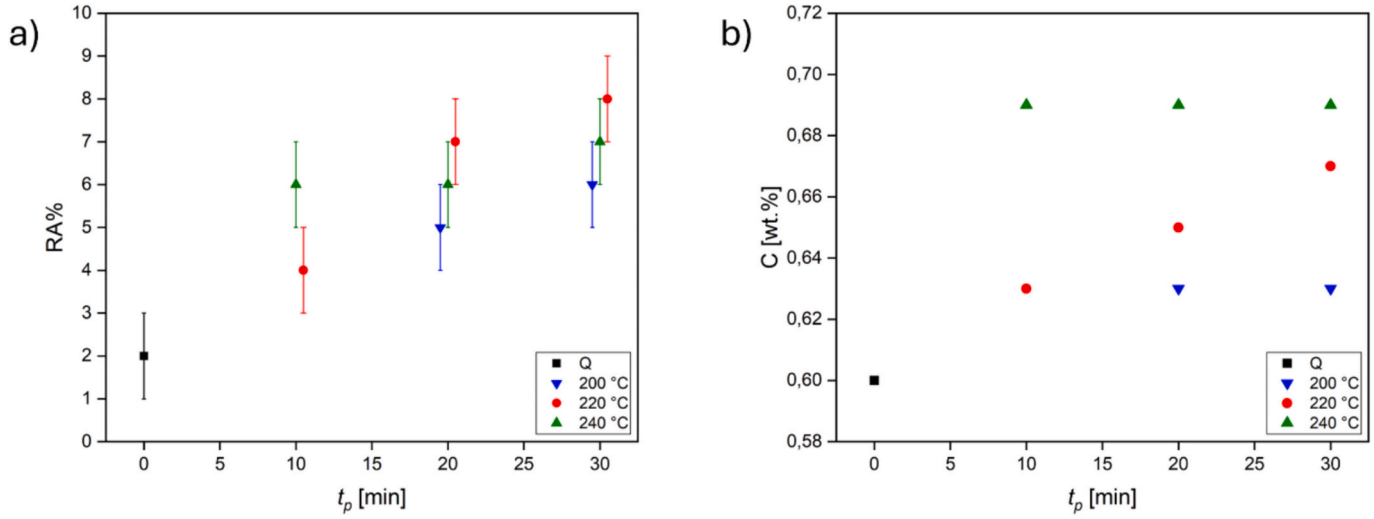

Fig. 13. XRD results. a) RA vs partitioning time B) Carbon content vs partitioning time. Please note that in Fig. 13a, results are shifted to improve clarity.

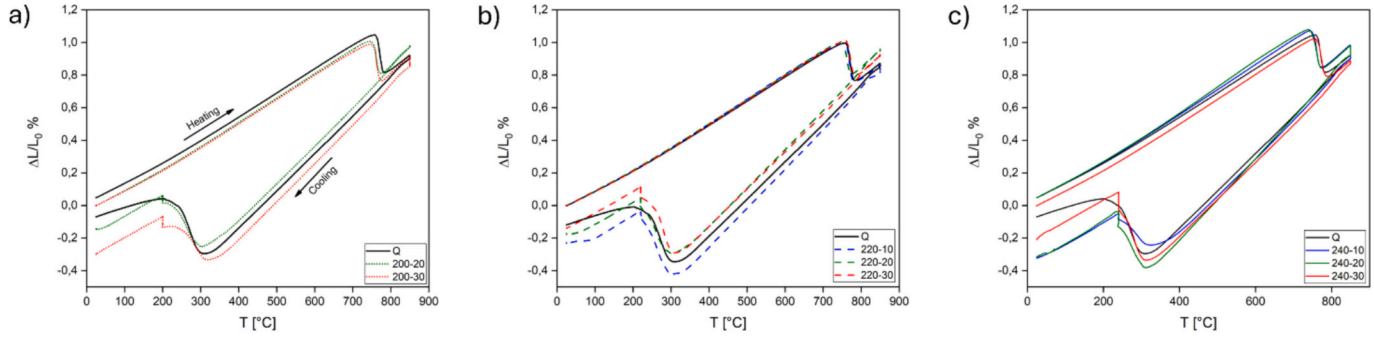

Fig. 14. Dilatometry curves for the QP samples partitioned at different temperatures: A) 200 °C, B) 220 °C, C) 240 °C.

$$m_{f_{\alpha'}} = m_{100\%\alpha'} * f_{\alpha'} + m_{100\%\gamma} * (1 - f_{\alpha'})$$

where $f_{\alpha'}$ is the fraction of martensite at room temperature and $m_{100\%\gamma}$ is the slope of the extrapolated curve for the 100% austenite case. $m_{f_{\alpha'}}$ is the slope of the interpolating curve at room temperature for the quenched sample and $m_{100\%\alpha'}$ is the unknown term in the equation.

– The initial fraction of austenite after quenching at different temperatures (200–220-240 °C) was computed by applying the lever rule between 100% γ extrapolated curve and the 100% α' reconstructed curve.

The computed austenite fractions after the first quenching in the Q sample were 7, 12, and 19 % for T_q of 200, 220, and 240 °C, respectively.

The formation of FM was identified through the variation in the slope observed in the dilatometric curves during the second quenching phase. Its fraction is computed by comparing its dilatation $\Delta L/L_0$ with the extrapolated 100% α' condition, with the following proportion:

$$(f_{FM})_{QP,RT} = (f_{\alpha'})_Q \frac{\left(\frac{\Delta L}{L_0}\right)_{QP,RT}}{\left(\frac{\Delta L}{L_0}\right)_{Q,RT}}$$

The highest FM fractions were observed in the 220–10 (8 %) and 220–20 (4 %) samples. Samples 200–30 and 220–30 showed lower FM

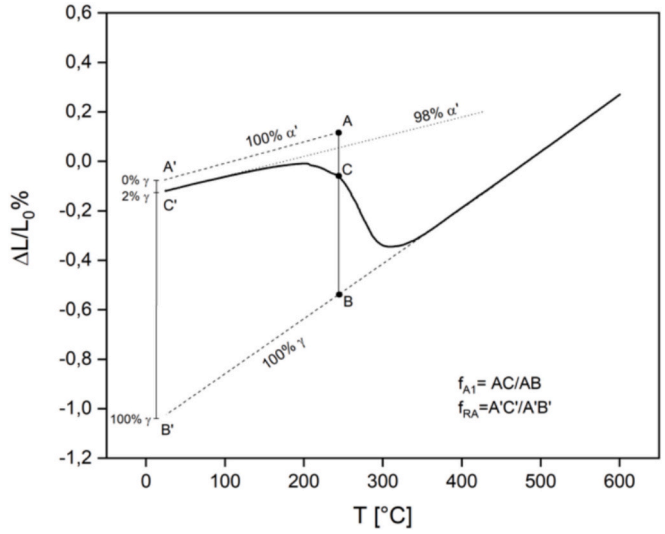

Fig. 15. Dilatometry curve processing for phase computation.

fractions (2 %) instead. Isothermal bainitic transformation may occur after the first quenching phase during the partitioning phase in both single- and dole-step QP treatments, and the presence of prior martensite accelerates the overall kinetics of bainite formation [19]. Multiple studies have observed through dilatometry that the occurrence of dilatations during isothermal holding can be ascribed more to bainitic transformation than to an increase in the lattice parameter owing to carbon enrichment [20,59,60].

In Fig. 16, the evolution of $\Delta L/L_0$ along t_p is plotted for samples that showed dilatation during partitioning. The dilatation values were normalized to zero through this rule: the time for dilatation as well as $\Delta L/L_0$ is set to zero when the sample reaches the minimum temperature during the quenching phase.

The sample 240–30, featured by a combination of both maximum partitioning time and temperature, showed the highest dilatation during isothermal holding, reaching 0.08 %. Sample 240–20 showed 0.03 % dilatation during holding. These samples were both quenched at 240 °C, featuring the highest initial austenite fraction after quenching, which might have undergone isothermal transformation, and the highest carbon partitioning. Samples 240–10, 200–30 and 220–30 instead, featured by a lower partitioning time/temperature, show a negligible dilatation, lower than 0.01 %. In this case, there is no reference sample to directly

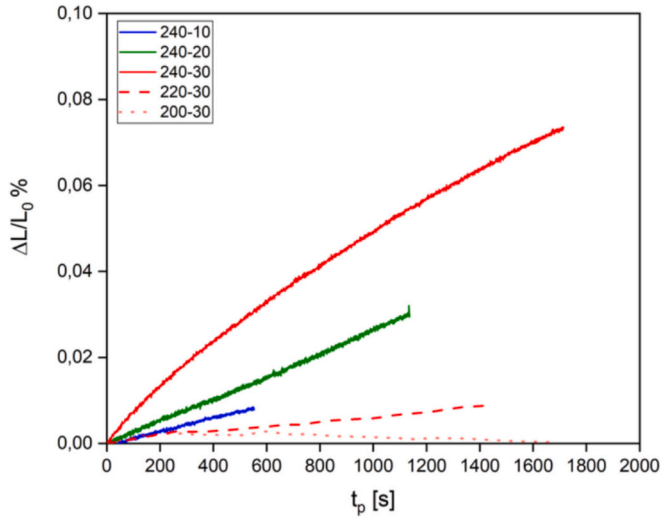

Fig. 16. Dilatation during isothermal partitioning for different samples.

compare this value with; thus, precise estimation of the final fraction of bainite can be complex. Several studies have attempted to establish a correlation between the level of dilatation during partitioning and the amount of bainite formed. Kumar et al. [61] observed for a Fe-0.25C-1.5Mn-1.5Si-0.25Mo-0.5Ni alloy that a 0.03 % dilatation corresponded to a 5 % volume fraction of bainite, while Findley et al. observed in a Fe-0.2C-3.51Mn-1.52Si-0.51Mo steel at a 0.01 % dilatation was correlated to a 1 % volume fraction of bainite [59]. The bainite fractions were calculated as follows:

$$f_B = f_{A1} - f_{FM} - f_{RA}$$

The bainite fraction was computed in the highest dilatation sample (240–30) as the difference between the initial austenite fraction after the first quenching phase and the computed FM and RA fractions.

This value was proportionally scaled in the other cases to quantify the amount of transformation obtained during isothermal treatment. Sample 240–30 shows a bainite fraction close to 12 %. Coherently, the resulting amounts computed with such a method for 220–30 and 240–10 cases, which show very little dilatation during partitioning, are very low (lower than 2 %). A summary of the microstructural features of the treated samples is presented in Table 4.

A partitionability map is proposed in Fig. 17 to highlight the different outcomes of QP as a function of the process parameters. The framework addresses the effectiveness of the treatment, knowing that the goal of the treatment is to obtain a martensite – austenite final microstructure. FM forming conditions are not acceptable because of the brittleness of such a phase [17]. Bainite-forming conditions are not optimal because this transformation occurs at the expense of RA. Nevertheless, the presence of bainite is generally not detrimental to the tensile properties. The following map proposes an optimal partitionability area for the selected alloy, where the partitioning time and temperature are high enough to avoid as much as possible FM formation, but low enough to avoid bainitic transformation, leading to a final microstructure composed of martensite and RA.

Two conditions, namely 220–30 and 240–30 were selected for further in-depth analyses. These two conditions feature the highest amount of RA among the different cases and with a high carbon content, without the presence of brittle FM. Moreover, they are featured by the same t_p, giving indications on the effects of T_p. SEM images of the QP samples are shown in Fig. 18. Fig. 18a shows the reference quenched sample with a fully martensitic microstructure: the microstructure is homogeneous along the observed area, and it is martensitic, confirming that the chosen cooling rate was greater than the critical rate for quenching in the selected material, which is consistent with the results of the dilatometry tests. Bainite, if present, is hardly distinguishable from martensite due to their morphological similarity [19]. RA is barely visible at these magnifications because of its small thickness, as observed previously in the literature [62]. On the other hand, QP samples (Fig. 18b,c) show regions more reactive to etching, similar to those reported for auto tempered low alloy medium C steels where precipitation of transition carbides within martensite is expected.

EBSD analysis, performed on sample 220–30 with the highest RA

Table 4
Summary of microstructural features in the different samples. *Determined by dilatometry, **measured using XRD.

Sample	FM* [vol%]	B* [vol%]	RA** [vol%]	a_γ [Å]	C [wt.%]
Q		–	2	3.584	0.60
200–20	2	–	5	3.585	0.63
200–30	2	–	6	3.585	0.63
220–10	8	–	4	3.585	0.63
220–20	4	–	7	3.586	0.65
220–30	2	<2 %	8	3.587	0.67
240–10	–	<2 %	6	3.588	0.69
240–20	–	6	6	3.588	0.69
240–30	–	12	7	3.588	0.69

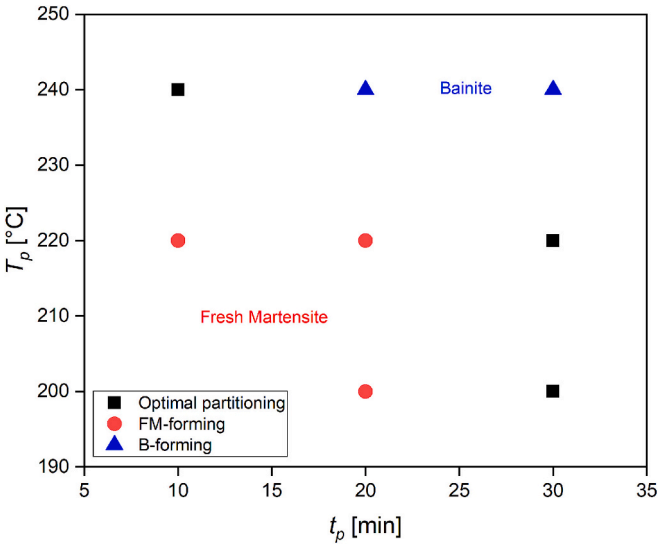

Fig. 17. Partitionability map for the selected QP treatments.

content, showed the presence of a fine distribution of RA in a martensitic matrix. A lower RA fraction was found compared to the XRD (~1 % vs 8 %) analysis because of the sensitivity to the surface preparation and the typical low thickness of RA compared to the selected step size of the EBSD analysis [62,63]. Typically, the percentage of retained austenite observed by EBSD is lower than that measured by XRD, as the resolution of the measurement (0.1 μm in this study) is insufficient to distinguish film-type austenite, which is usually nanometric and may also be present in the cases shown. The dimensions of the RA grains were mostly sub-micrometric, and they were located at the grain boundaries and in the interlath regions. This distribution is preferable in QP steels because a fine RA dispersion inside the microstructure has been identified as the best condition to maximize the effectiveness of the treatment on the mechanical properties [64]. The presence of clusters of austenite grains characterized by a common orientation, as shown in Fig. 19, is indicative of the retained nature of austenite, which continues to possess the orientation of the PAG to which it originally belonged.

Tensile tests were performed under selected conditions, namely 220–30 and 240–30, as well as the as-sintered (AS) V1440 condition, which was used as a reference. The tensile properties of the specimens are listed in Table 5.

The application of QP treatments introduced a high UTS (higher than 1150 MPa) as expected from the presence of a hard martensitic matrix. The 220–30 sample, featuring lower tempering, showed a higher UTS than 240–30 [20]. The ductility is low (2–4 %) because of the porous structure of the specimens, which is typically responsible for such poor results [65–67]. Nevertheless, the UTS/YS ratio is high in the different conditions, especially in the 220–30 case, where it reaches 1.7, and a high strain hardening in the material might lead to potentially good ductility in the case of a fully dense material. The AS sample showed lower tensile strength (750 MPa), coupled with slightly higher ductility, as expected by the presence of a non-martensitic, and thus softer, multiphase microstructure, as shown in Fig. 20.

The fracture surfaces of the 220–30 and 240–30 specimens were

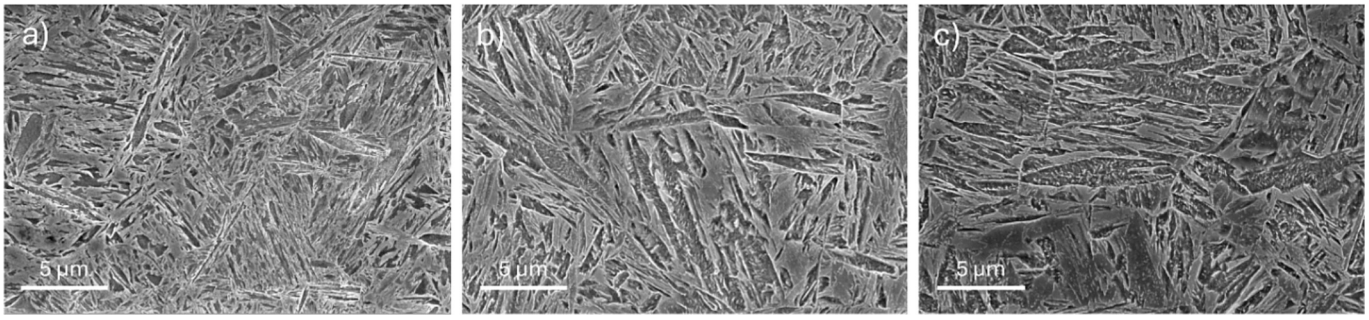

Fig. 18. SEM pictures highlighting the martensitic microstructure for different conditions: a) Quenched (Q), b) 220–30, c) 240–30.

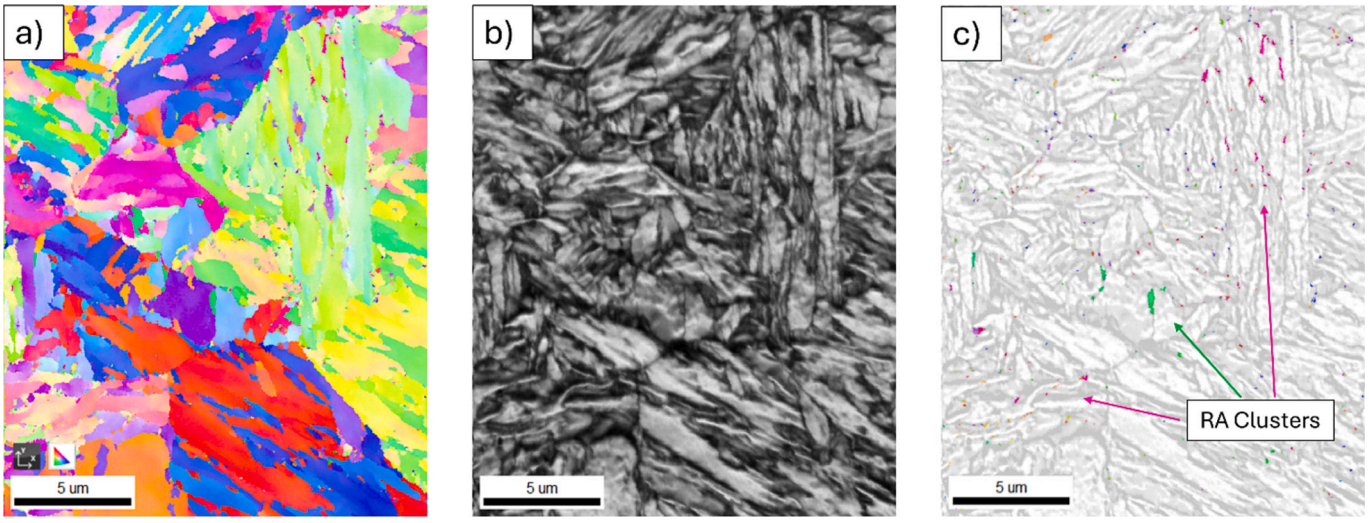

Fig. 19. EBSD analysis on 220–30 sample: a) Inverse Pole Figure (IPF) b) Image Quality (IQ), c) Retained austenite distribution in the martensitic matrix (IPF + Band Contrast).

Table 5
Tensile properties of the QP-treated materials, and the as-sintered (AS) condition.

Sample	YS [MPa]	UTS [MPa]	ε_{max} [%]	UTS/YS
220–30	732	1231	2	1.7
240–30	892	1151	4	1.3
AS	544	750	6	1.4

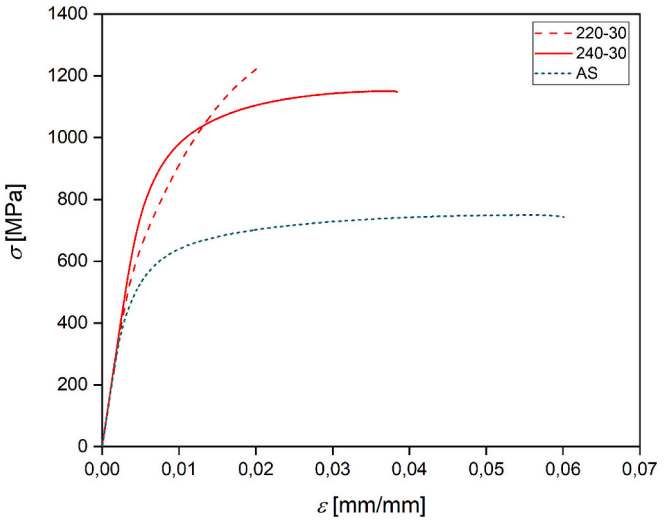

Fig. 20. Representative tensile curves of samples in the QP and in the as-sintered (AS) condition.

analyzed to investigate the failure mechanisms at the microscopic level. AS sample was also tested for comparison. SEM images are shown in Fig. 21.

Consistent with previous analyses, the fracture surfaces showed the presence of an incompletely densified structure, characterized by a distribution of porosity along the entire section (Fig. 21c). The fracture appeared macroscopically brittle under all the different conditions. Consistently, it can be seen that at the microscopic level, specimen 220–30 (Fig. 21a) did not show ductility and dimples. Sample 240–30 (Fig. 21b) showed some limited inter-pore ductility zones. In contrast, specimen AS (Fig. 21c) is characterized by the presence of dimples in the inter-pore zones, a sign of increased plastic deformation before fracture. The failure mechanism can be explained as follows: the porosity zones, which are expanded in the tensile process, progressively decrease the cross-section of the material, which is gradually strained. In cases 220–30, 240–30, rupture occurred under these conditions because of the limited ductility of the poorly tempered martensite. The AS specimen, which has a more ductile microstructure, shows increased local ductility and deeper dimples, and hence a higher elongation at break.

4. Discussion

As-sintered materials feature relevant variations in their microstructural and mechanical properties depending on the processing conditions, as observed above. The pivotal factor determining the development of the sintered specimens is the massive variation in the carbon content at high temperatures as a consequence of the processing atmosphere of debinding and sintering, as shown in Fig. 4. The initial increase from debinding in inert atmospheres is due to the incomplete burnout of the polymer deposited during printing. The consumption of carbon in the solution might be favored by different factors:

- The accelerated removal of the organic residue in the presence of atmospheric oxygen and metallic oxides that eliminate an alternative source of carbon, which could have preserved that of the alloy [68,69].
- The high specific surface area is due to the reduced average size of the powder, which increases the reaction exchange area and minimizes the diffusion path for carbon from the particle center to the surface.
- The presence of oxygen in the atmosphere that prevents the consumption of this reactant, which is otherwise limited to the oxidation of the metal.

After sintering, decarburization was observed in all samples to a similar extent. This phenomenon occurs in ferrous alloys due to the carbothermal reduction of iron oxides at temperatures above A_1, according primarily, but not solely, to the following reaction:

$$3Fe_2O_3 + C \rightarrow 2Fe_3O_4 + CO$$

Decarburization is faster below *TG* (i.e. A_3 at C = 0 wt%) and progressively slows down owing to the $\alpha \rightarrow \gamma$ transformation, which is correlated with a reduction in the carbon diffusion rate that limits the amount of reactant at the surface [70,71]. For the considered chemical composition, the *TG* is close to 850 °C (Fig. 1), and only partial decarburization of the surface region should be observed in a non-oxidizing atmosphere [72]. Therefore, the terminal amount of carbon in solution is influenced by its initial concentration (after debinding), the amount of organic residue, and the extent of the oxide scale on the particles. As expected, the air-debinded samples underwent an almost complete loss of carbon, while they were partially retained in Ar- and vacuum-debinded specimens (see Fig. 4). However, only the vacuum-debinded parts maintain sufficient carbon, especially in the surface region, to prevent the massive formation of the δ phase during SSS, thus justifying the homogeneous microstructure observed in Fig. 5. In the case of SLPS (V1510), the carbon content is minimal even in the case of vacuum-treatments: the liquid fraction can solubilize a larger fraction of oxygen, which is responsible for further decarburization due to carbothermic reduction after solidification during the cooling process. Fig. 22 displays the volume fraction map of ferrite at sintering temperatures, confirming the formation of relevant fractions of such phase for strongly

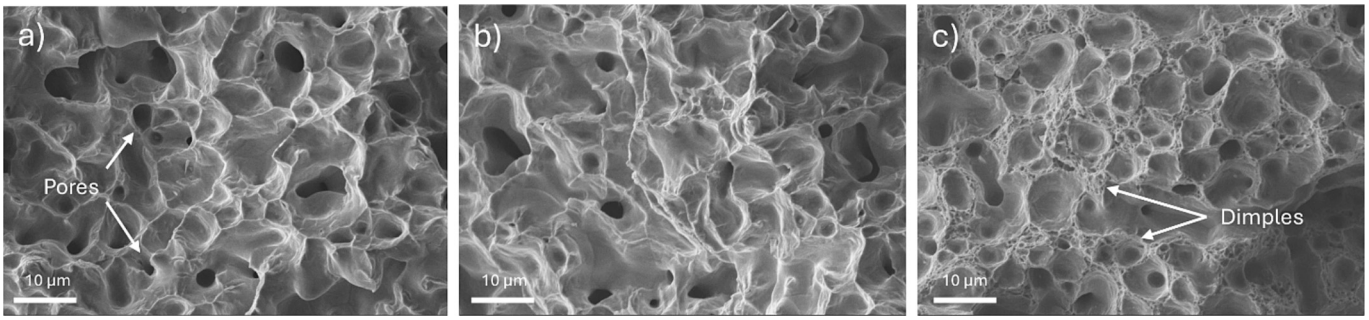

Fig. 21. SEM pictures of the fracture surfaces. a) 220–30, b) 240–30, c) AS.

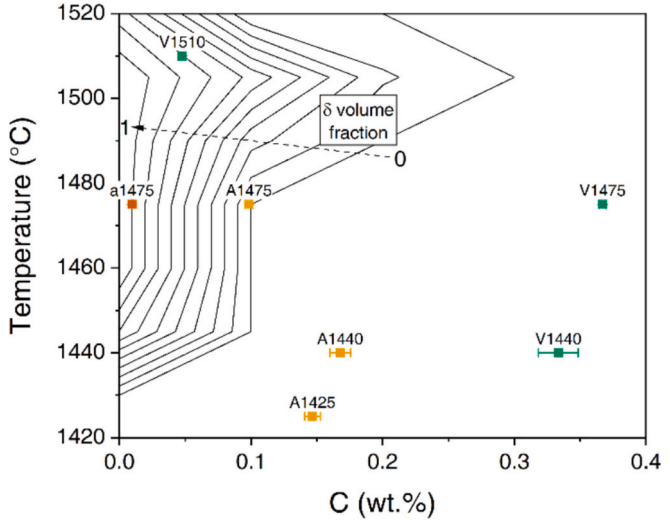

Fig. 22. Delta ferrite volume fraction map with dependence on temperature and carbon content.

decarburized components. Interestingly, ferritic grains were observed as well in all Ar-debinded specimens (see Fig. 5), although the simulation predicts the δ phase formation only for parts sintered at 1475 °C. Such results it can be easily justified by considering that decarburization, thus the carbon content, does not occur to the same extent in the entirety of the printed volume, but on exposed surfaces preferentially, as denoted in the micrography of A1425. LECO measurements determine the average carbon content in the bulk of the material; thus, it cannot resolve concentration gradients within the microstructure.

Fig. 23 shows the straightforward correlation between the overall carbon content and microhardness. Carbon is an austenite stabilizer; its loss facilitates the formation of δ_F at high temperatures during heating, PF/GB at higher temperatures during cooling, and limiting/preventing the precipitation of cementite, as observed in the metallographies. The importance of the carbon content on the mechanical properties was confirmed by the tensile properties of the vacuum-debinded samples presented in Fig. 10. Indeed, in the case of V1440, lower carbon content in the solid solution and higher amounts of δ/α ferrite are correlated to a reduction in the yield and tensile strength, while the ductility is improved.

V1440 was selected as the optimal condition for further processing

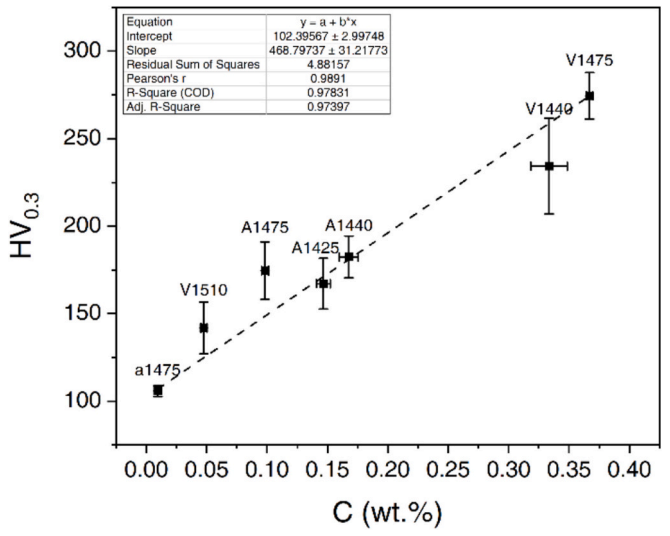

Fig. 23. Correlation among microhardness and carbon content.

for several reasons. It retained a sufficient amount of carbon, although V1475 was closer to the theoretical content of AISI 4340, so that δ ferrite formation was prevented and the mechanical properties should not be hindered, which was not achieved under air- and Ar-debinded conditions. The geometrical accuracy was consistent throughout different printed batches, which was not the case for SLPS (V1510) owing to excessive liquid formation and V1475, which seemed to suffer from warping in some cases. The sintering temperature was the lowest among the vacuum-debinded specimens, thus reducing the risk of liquid formation and granting savings in time, energy, and costs for potential industrial production. Nonetheless, it should be noted that even V1440 suffers from a series of flaws that also affect post-processed conditions. Indeed, densification is limited, and residual porosity is present in the entirety of the material and anisotropically distributed according to the layerwise printing process, as observed in Fig. 21c as well as in the literature [44,73]. Therefore, lower mechanical performance should be expected, especially in the case of tensile testing, with respect to fully densified components obtained from conventional manufacturing processes [65]. Nevertheless, the application of quenching and partitioning is meant to obtain a controlled microstructure with improved tensile properties. With respect to traditional quenching and tempering treatments indeed, the presence of retained austenite in the QP condition has the additional ability to increase ductility through strain-induced transformation, possibly partially offsetting the limits given by the porosity resulting from the building technique.

The reduction in the carbon concentration due to decarburization is reflected in the variation of the critical temperatures. Dilatometry showed an increase in the critical temperatures, consistent with the decrease in carbon content during the additive manufacturing process, as shown in Fig. 14. The carbon concentration computed starting from the experimental M_s obtained through dilatometry was consistent with that measured by combustion analysis, confirming the occurrence of the decarburization process. QP treatments were designed through the application of CCE, considering the new chemical composition, and optimized through Celada-Casero et al. [17]. The chosen t_p and T_p are critical for optimizing the microstructural development of the material. Moreover, because the treatment is based on carbon diffusion, competitive phenomena such as the precipitation of transition carbides must be controlled. This is usually achieved by the addition of Si to the alloy, which suppresses carbide precipitation. However, since the studied steel is a commercial one, it does not have a tailored chemistry for this treatment, and as a result, the full potential of the treatment cannot be achieved. Nevertheless, the proposed treatments were able to stabilize an acceptable fraction (4–8 %) of RA, indicating an effective application of QP to the selected steel. The carbon content in austenite (Fig. 13) reflects the increase in austenite lattice parameter a_γ owing to its diffusion from the supersaturated martensite to austenite during partitioning. The QP conditions show an increased a_γ (3.585–3.588 Å) compared to the as-quenched sample, which also showed a small fraction of RA (2 %) with a lower lattice parameter (3.584 Å), and thus low stability. Although the QP-treated samples show a limited variability in a_γ and thus in carbon concentration (0.63–0.69), it can be observed that higher partitioning times and temperatures generally lead to higher carbon concentration in austenite and thus higher stability.

Dilatometry curves showed that phase transformations other than martensite formation were avoided during quenching. The generation of FM was observed during the second quenching step in the 200–20, 220–10, and 220–20 cases - those with the lowest T_p and t_p – indicating an insufficient austenite stabilization during the partitioning step. FM must be avoided because it dramatically degrades the tensile properties of the material [16,18]. The 240–20 and 240–30 specimens instead featured a non-negligible dilatation during partitioning, which can be ascribed to isothermal bainite [19,20,60]. The proposed partitionability map showed a tiny optimal operative window for a theoretically optimal QP application to avoid undesired phase transformations. 220–30 and 240–30 samples showed the highest amount of RA at room temperature

and are differentiated only by T_p; thus, they are identified as the best conditions for successive analysis. The SEM images showed the presence of a martensitic matrix in the different QP cases. EBSD analysis was performed on specimen 220–30, characterized by the highest fraction of RA, which is fine in size and distributed both in the interlaths and at the GBs. Clusters of RA with the same crystallographic orientation were observed, indicating that they belong to the same PAG [17,62].

Tensile tests were conducted on the selected conditions 220–30, 240–30, featured by the highest RA fraction and compared with the AS sample used as a reference. AS specimen exhibited UTS above 700 MPa with a ductility of 6 %. QP specimens exhibited excellent mechanical properties, reaching a UTS above 1100 MPa. The highest ductility (4 %) was obtained in the 240–30 specimen. The low ductility was due to the widespread porosity in the material owing to the limited densification, which reduces the resistant section and creates weak zones for crack propagation [65,74]. Nevertheless, the properties obtained are still competitive regarding a component made by additive manufacturing containing such level of porosity. The fracture surfaces appear macroscopically brittle under all the conditions. While the AS sample was characterized by the presence of dimples in the zones between the porosities, the QP samples showed a more microscopically brittle fracture surface. Nevertheless, the increased mechanical strength is coupled with a limited loss of ductility. Moreover, work hardening was not reduced by the heat treatment but remained high, as shown by the UTS/YS ratio, which ranged between 1.3 and 1.7. These features are consistent with the presence of a fraction of RA that enhances the UTS but decreases the YS and ductility through its deformability and strain-induced transformation [20].

It can be inferred that the application of QP treatment to the selected material shows a propensity for obtaining high strength accompanied by a non-proportional decrease in ductility. The optimization of heat treatments should be accompanied by an effective densification during the sintering phase in order to ensure an excellent combination of mechanical properties. As can be seen from the experimental procedure, the building technique and sequent QP heat treatment are linked because the treatment must be optimized according to the concentration of carbon present after sintering. The range of mechanical properties that can be obtained depends on the carbon content because the mechanical properties of martensite are a function of carbon concentration. It can be concluded that the building technique (BJT) and heat treatment (QP) should be optimized synergistically to ensure optimal results at the end of treatment. Although some criticality has emerged in densification and chemical composition control after sintering, the foundation is laid on knowledge of the effect of BJT on commercial steels, and the mechanical properties can be increased by the application of QP.

5. Conclusions

This study shows the possibility of effectively applying post-processing thermal treatments, in this case, quenching and partitioning, on commercial AISI 4340 steel produced by binder jetting to effectively tune the mechanical properties after sintering. This study demonstrated that debinding atmospheres and sintering parameters are pivotal factors that influence the initial microstructural characteristics, chemical composition, and mechanical performance of binder-jetted samples of 4340 low-alloy steel. Quenching and partitioning treatments were successfully applied to components obtained by the optimized building cycle to control the development of two-phase martensite and austenite microstructures, thus tailoring the mechanical properties of the final component. Nonetheless, a reduction in printing-dependent defects is of primary importance for an optimal result because they strongly affect the behavior of the material, regardless of the subsequent heat treatments.

This study demonstrated the following:

- Densification and shrinkage rates remained constant, except for specimens obtained by air-debinding and super-solidus liquid-phase sintering, owing to the formation of relevant fractions of δ ferrite and liquid, respectively. Nonetheless, in the former case, oxide inclusions were present in the entire microstructure, whereas in the latter case, severe geometrical distortions were observed after sintering.
- The vacuum-debinded specimens in the as-sintered state exhibited the most homogeneous microstructures, consisting predominantly of granular bainite, resulting in superior hardness and tensile strength compared to their air- and argon-debinded counterparts, although the presence of residual porosity limited the maximum elongation during tensile testing.

– The carbon content played a pivotal role in the microstructure evolution and property optimization, as evidenced by the correlation between the residual carbon concentration, phase distribution, and hardness. Decarburization occurred mostly during the heating stage of sintering, promoted by the carbothermic reaction, leading to oxide reduction. Vacuum debinding was identified as optimal, as it prevented excessive oxidation and left a larger fraction of organic carbon residue, which prevented the complete consumption of carbon in the solid solution. Especially, the specimen sintered at 1440 °C in vacuum was found to be the optimized condition that maximizes density (92 % of densification) keeping a satisfactory carbon concentration (0.34 %), and thus was selected as starting condition for QP treatments. The design of QP treatments is influenced by the building technique because the decarburization occurring during debinding and sintering steps affected the critical temperatures. Therefore, the building parameters and QP treatments must be tailored synergistically to maximize the effectiveness of heat treatment by controlling the microstructure.
– Different single-step QP treatments were successfully applied under the selected optimal as-sintered conditions. Fractions of RA between 4 and 8 % were stabilized in a martensitic matrix. The samples with the highest RA contents were treated at 220 °C and 240 °C for 30 min (220–30 and 240–30, respectively). Fresh martensite and bainite were detected in the optimal conditions. A partitionability map was proposed to determine the optimal process parameters for the maximum effectiveness of the treatment.
– High tensile properties were obtained as the QP samples reached a UTS of 1151 MPa in sample 240–30 and 1231 MPa in sample 220–30. These values are improved compared with the as-sintered condition, which reached 750 MPa. Ductility in all samples was low, 4 % in 240–30 and 2 % in 220–30. This behavior was attributed to the high porosity after sintering; indeed, the ductility is already low (6 %) in the as-sintered condition.

These results verified the possibility of controlling the microstructure of AISI 4340 commercial steel through quenching and partitioning to ensure high mechanical properties despite the limitations of the additive manufacturing technique. These findings underscore the importance of controlled building and processing conditions in tailoring the microstructural and mechanical properties of sintered components for advanced engineering applications. Future work should focus on the production process to determine the optimal set of parameters for proper densification, which would certainly improve the mechanical properties of as-sintered and thermally treated parts. Subsequent heat treatments should be optimized according to the final carbon concentration to ensure proper final properties.

CRediT authorship contribution statement

M. Belfi: Writing – original draft, Methodology, Investigation, Conceptualization. **M. Mariani:** Writing – original draft, Methodology, Investigation, Conceptualization. **P. Martin:** Writing – review & editing, Methodology, Investigation. **M. Santofimia:** Writing – review & editing, Supervision, Resources, Methodology. **A. Gruttadauria:** Writing –

review & editing, Supervision. **F. Deirmina:** Writing – review & editing, Resources. **N. Lecis:** Supervision, Resources. **S. Barella:** Writing – review & editing, Supervision, Resources.

Declaration of competing interest

The authors declare that they have no known competing financial interests or personal relationships that could have appeared to influence the work reported in this paper.

Acknowledgements

The authors acknowledge E. Bettini from Sandvik AB, R. Beltrami from LECO ITALY Srl, and L. Krachler for the support provided to the experimental activity. Special thanks to the Materials Science and Engineering Department (TU Delft) for experimental support, especially to C. Kwakernaak, R. Huizenga and N. Geelhofs for their highly valuable technical support and constructive and helpful discussions.

The authors would like to acknowledge the "Functional Sintered Materials (Funtasma)" Interdepartmental Laboratory of Politecnico di Milano, where this research activity was developed.

Appendix A

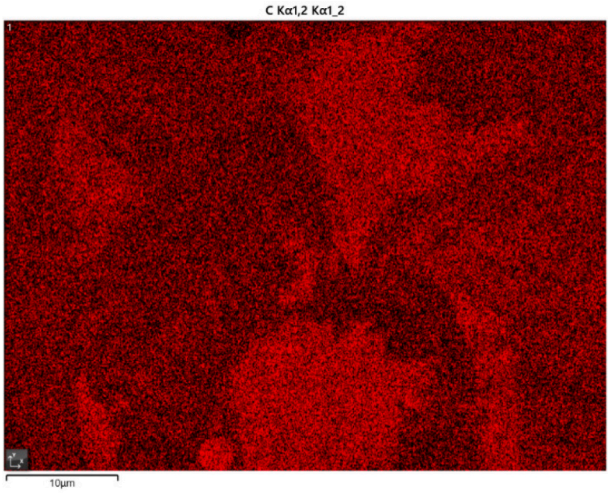

Fig. 24. EDX map of the carbon concentration for the high magnification image of the V1440 specimen presented in Fig. 7.

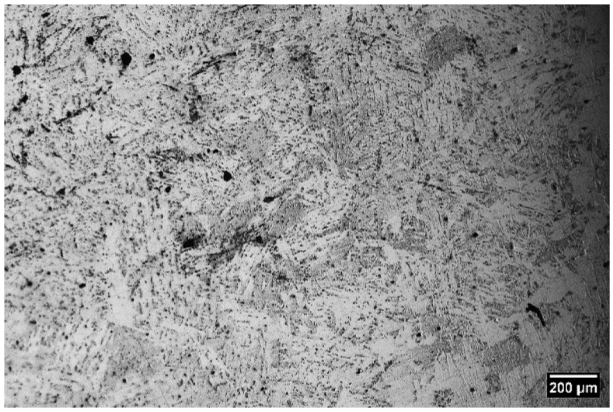

Fig. 25. Metallography of the V1510 sintered specimen.

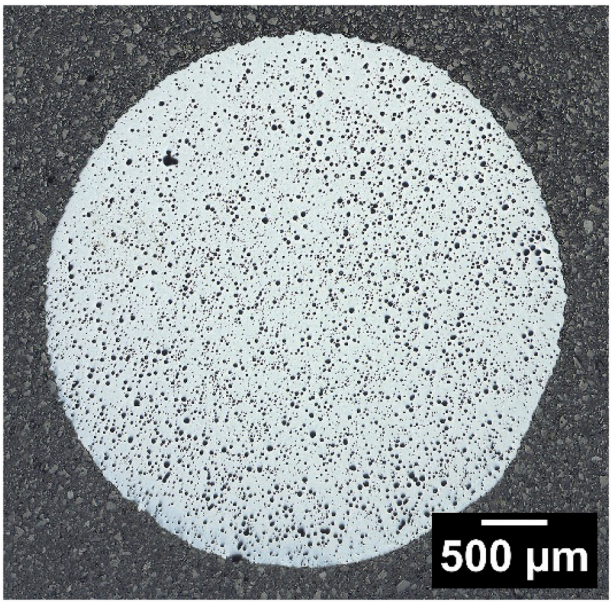

Fig. 26. Metallography of a dilatometry specimen.

Data availability

Data will be made available on request.

References

[1] M. Mariani, N. Lecis, A. Mostafaei, Binder jetting-based metal printing, in: H.Z. Yu, N. Tuncer, Z. Feng (Eds.), Solid-State Met. Addit. Manuf. Physics, Process. Mech. Prop, Appl., John Wiley & Sons Inc, 2024, pp. 339–360.

[2] Y. Tomita, Development of fracture toughness of ultrahigh strength low alloy steels for aircraft and aerospace applications, Mater. Sci. Technol. 7 (1991) 481–489, https://doi.org/10.1179/mst.1991.7.6.481.

[3] K.J.B. Ribeiro, R.R.M. de Sousa, F.O. de Araújo, R.A. de Brito, J.C.P. Barbosa, C. Alves, Industrial application of AISI 4340 steels treated in cathodic cage plasma nitriding technique, Mater. Sci. Eng. A 479 (2008) 142–147, https://doi.org/10.1016/j.msea.2007.06.033.

[4] R. Bag, A. Panda, A.K. Sahoo, R. Kumar, A comprehensive review on AISI 4340 hardened steel: emphasis on industry implemented machining settings, implications, and statistical analysis, Int. J. Integr. Eng. 12 (2020) 61–82, https://doi.org/10.30880/ijie.2020.12.08.007.

[5] W.L. Holshouser, Failure in aircraft parts made of ultra-high-strength steel, J. Fail. Anal. Prev. 22 (2022) 2479–2486, https://doi.org/10.1007/s11668-022-01547-x.

[6] W.-S. Lee, T.-T. Su, Mechanical properties and microstructural features of AISI 4340 high-strength alloy steel under quenched and tempered conditions, J. Mater. Process. Technol. 87 (1999) 198–206, https://doi.org/10.1016/S0924-0136(98)00351-3.

[7] V.K. Euser, A.J. Clarke, J.G. Speer, Rapid tempering: opportunities and challenges, J. Mater. Eng. Perform. 29 (2020) 4155–4161, https://doi.org/10.1007/s11665-020-04946-z.

[8] A.J. Clarke, J. Klemm-Toole, K.D. Clarke, D.R. Coughlin, D.T. Pierce, V.K. Euser, J. D. Poplawsky, B. Clausen, D. Brown, J. Almer, P.J. Gibbs, D.J. Alexander, R. D. Field, D.L. Williamson, J.G. Speer, G. Krauss, Perspectives on quenching and tempering 4340 steel, Metall. Mater. Trans. A 51 (2020) 4984–5005, https://doi.org/10.1007/s11661-020-05972-1.

[9] C. Zhu, X.Y. Xiong, A. Cerezo, R. Hardwicke, G. Krauss, G.D.W. Smith, Three-dimensional atom probe characterization of alloy element partitioning in cementite during tempering of alloy steel, Ultramicroscopy 107 (2007) 808–812, https://doi.org/10.1016/j.ultramic.2007.02.033.

[10] O. Tikhe, P. Doiphode, U. Nichul, R. Singh, V. Hiwarkar, Development of optimized mechanical properties of AISI 4340 steel: role of quenching and partitioning process, Met. Mater. Int. 29 (2023) 2216–2227, https://doi.org/10.1007/s12540-022-01375-6.

[11] J. Speer, D.K. Matlock, B.C. De Cooman, J.G. Schroth, Carbon partitioning into austenite after martensite transformation, Acta Mater. 51 (2003) 2611–2622, https://doi.org/10.1016/S1359-6454(03)00059-4.

[12] A.J. Clarke, J.G. Speer, M.K. Miller, R.E. Hackenberg, D.V. Edmonds, D.K. Matlock, F.C. Rizzo, K.D. Clarke, E. De Moor, Carbon partitioning to austenite from martensite or bainite during the quench and partition (Q&P) process: a critical assessment, Acta Mater. 56 (2008) 16–22, https://doi.org/10.1016/j.actamat.2007.08.051.

[13] S. Ebner, R. Schnitzer, E. Maawad, C. Suppan, C. Hofer, Influence of partitioning parameters on the mechanical stability of austenite in a Q&P steel: a comparative in-situ study, Materialia 15 (2021) 101033, https://doi.org/10.1016/j.mtla.2021.101033.

[14] E. De Moor, J.G. Speer, D.K. Matlock, D.N. Hanlon, Effect of retained austenite on tensile behavior of AHSS revisited, Mater. Sci. Technol. Conf. Exhib. MS T'11 1 (2011) 568–579.

[15] J.G. Speer, E. De Moor, K.O. Findley, D.K. Matlock, B.C. De Cooman, D. V. Edmonds, Analysis of microstructure evolution in quenching and partitioning automotive sheet steel, Metall. Mater. Trans. A Phys. Metall. Mater. Sci. 42 (2011) 3591–3601, https://doi.org/10.1007/s11661-011-0869-7.

[16] D. De Knijf, C. Föjer, L.A.I. Kestens, R. Petrov, Factors influencing the austenite stability during tensile testing of quenching and partitioning steel determined via in-situ Electron backscatter diffraction, Mater. Sci. Eng. A 638 (2015) 219–227, https://doi.org/10.1016/j.msea.2015.04.075.

[17] C. Celada-Casero, C. Kwakernaak, J. Sietsma, M.J. Santofimia, The influence of the austenite grain size on the microstructural development during quenching and partitioning processing of a low-carbon steel, Mater. Des. 178 (2019) 107847, https://doi.org/10.1016/j.matdes.2019.107847.

[18] J. Mola, B.C. De Cooman, Quenching and partitioning (Q&P) processing of martensitic stainless steels, Metall. Mater. Trans. A 44 (2013) 946–967, https://doi.org/10.1007/s11661-012-1420-1.

[19] S. Dhara, S.M.C. van Bohemen, M.J. Santofimia, Isothermal decomposition of austenite in presence of martensite in advanced high strength steels: a review, Mater. Today Commun. 33 (2022) 104567, https://doi.org/10.1016/j.mtcomm.2022.104567.

[20] A. Navarro-López, J. Hidalgo, J. Sietsma, M.J. Santofimia, Unravelling the mechanical behaviour of advanced multiphase steels isothermally obtained below Ms, Mater. Des. 188 (2020) 108484, https://doi.org/10.1016/j.matdes.2020.108484.

[21] I. Miettunen, S. Ghosh, M.C. Somani, S. Pallaspuro, J. Kömi, Competitive mechanisms occurring during quenching and partitioning of three silicon variants of 0.4 wt.% carbon steels, J. Mater. Res. Technol. 11 (2021) 1045–1060, https://doi.org/10.1016/j.jmrt.2021.01.085.

[22] S.Y.P. Allain, S. Aoued, A. Quintin-Poulon, M. Gouné, F. Danoix, J.C. Hell, M. Bouzat, M. Soler, G. Geandier, In situ investigation of the iron carbide precipitation process in a Fe-C-Mn-Si Q & P steel, Materials (Basel). 11 (2018) 1087, https://doi.org/10.3390/ma11071087.

[23] B. Kim, J. Sietsma, M.J. Santofimia, The role of silicon in carbon partitioning processes in martensite/austenite microstructures, Mater. Des. 127 (2017) 336–345, https://doi.org/10.1016/j.matdes.2017.04.080.

[24] S. Barella, M. Belfi, A. Gruttadauria, C. Liu, Y. Peng, Metallurgical and mechanical investigation on single-step quenching and partitioning thermal treatments on commercial low alloyed 30MnV6 steel, Metall. Mater. Trans. A Phys. Metall. Mater. Sci. (2023) 12–14, https://doi.org/10.1007/s11661-023-07262-y.

[25] S. Barella, M. Belfi, A. Gruttadauria, P. Cetto, Influence of quenching and partitioning on the mechanical properties of low silicon 33MnCrB5 boron steel, Steel Res. Int. 95 (2023) 2300622.

[26] S. Barella, A. Gruttadauria, J.T.O. Menezes, E.M. Castrodeza, S.E. Quaini, C. Pelligra, E.A. McNally, The reliability of single-step and double-step quench and partitioning heat treatments on an AISI 420A low carbon martensitic stainless steel, Metall. Mater. Trans. A Phys. Metall. Mater. Sci. 54 (2023) 3957–3972, https://doi.org/10.1007/s11661-023-07145-2.
[27] A.J. Coleman, K. Murray, M. Kearns, T.A. Tingskog, B. Sanford, E. Gonzalez, Effect of Particle Size Distribution on Processing and Properties of Metal Injection Moulded 4140 and 4340, in: Proceedings of the 2011 International Conference on Powder Metallurgy and Particulate Materials, PowderMet, 2011, pp. 401–412. https://api.semanticscholar.org/CorpusID:201914199.
[28] H. Nakayama, T. Toda, H. Kyogoku, S. Komatsu, Effect of Debinding conditions on the carbon content of sintered 4340 alloy compacts by metal injection molding, J. Japan Soc. Powder Powder Metall. 43 (1996) 368–372, https://doi.org/10.2497/jjspm.43.368.
[29] A.-F. Gil-Plazas, J.-D. Rubiano-Buitrago, L.-A. Boyacá-Mendivelso, L.-K. Herrera-Quintero, Solid-state and super solidus liquid phase sintering of 4340 steel SLM powders shaped by fused filament fabrication, Rev. Fac. Ing. 31 (2022) e13913, https://doi.org/10.19053/01211129.v31.n60.2022.13913.
[30] P. Nandwana, R. Kannan, D. Siddel, Microstructure evolution during binder jet additive manufacturing of H13 tool steel, Addit. Manuf. 36 (2020) 101534, https://doi.org/10.1016/j.addma.2020.101534.
[31] R. Kannan, P. Nandwana, Predicting sintering window during supersolidus liquid phase sintering of steels using feedstock analysis and CALPHAD, Mater. Lett. 304 (2021) 130648, https://doi.org/10.1016/j.matlet.2021.130648.
[32] Y. Lee, P. Nandwana, S. Simunovic, Powder spreading, densification, and part deformation in binder jetting additive manufacturing, Prog. Addit. Manuf. 7 (2021) 1–15, https://doi.org/10.1007/s40964-021-00214-1.
[33] I. Rishmawi, A. Rogalsky, M. Vlasea, A. Molavi-Kakhki, Comparison of the master sinter curves of water- and gas-atomized AISI 4340 low-alloy steel in binder jetting additive manufacturing, Addit. Manuf. 48 (2021) 102381, https://doi.org/10.1016/j.addma.2021.102381.
[34] M. Yang, M.K. Keshavarz, M. Vlasea, A. Molavi-Kakhki, M. Laher, Supersolidus liquid phase sintering of water-atomized low-alloy steel in binder jetting additive manufacturing, Heliyon 9 (2023) e13882, https://doi.org/10.1016/j.heliyon.2023.e13882.
[35] M. Yang, M.K. Keshavarz, M. Vlasea, A. Molavi-Kakhki, Towards full-dense high geometric fidelity parts via binder jetting and controlled sintering, J. Manuf. Process. 115 (2024) 180–191, https://doi.org/10.1016/j.jmapro.2024.02.028.
[36] A.J. Rayner, R.W. Cooke, I.W. Donaldson, S.F. Corbin, D.P. Bishop, Binder Jet Printing AISI 5120 Chromium Steel Powder, Metall. Mater. Trans. A 54 (2023) 1271–1285, https://doi.org/10.1007/s11661-023-06983-4.
[37] J. Liu, R. Kannan, D. Zhang, T. Liu, P. Nandwana, A. Devaraj, Multi-scale characterization of supersolidus liquid phase sintered H13 tool steel manufactured via binder jet additive manufacturing, Addit. Manuf. 56 (2022) 102834, https://doi.org/10.1016/j.addma.2022.102834.
[38] J.O. Andersson, T. Helander, L. Höglund, P. Shi, B. Sundman, Thermo-Calc & DICTRA, computational tools for materials science, Calphad Comput. Coupling Phase Diagrams Thermochem. 26 (2002) 273–312, https://doi.org/10.1016/S0364-5916(02)00037-8.
[39] L. Lutterotti, Total pattern fitting for the combined size-strain-stress-texture determination in thin film diffraction, Nucl. Instruments Methods Phys. Res. Sect. B Beam Interact. with Mater. Atoms 268 (2010) 334–340, https://doi.org/10.1016/j.nimb.2009.09.053.
[40] N.H. Van Dijk, A.M. Butt, L. Zhao, J. Sietsma, S.E. Offerman, J.P. Wright, S. Van Der Zwaag, Thermal stability of retained austenite in TRIP steels studied by synchrotron X-ray diffraction during cooling, Acta Mater. 53 (2005) 5439–5447, https://doi.org/10.1016/j.actamat.2005.08.017.
[41] M. Zago, N. Lecis, M. Mariani, I. Cristofolini, Analysis of the causes determining dimensional and geometrical errors in 316L and 17-4PH stainless steel parts fabricated by metal binder jetting, Int. J. Adv. Manuf. Technol. 132 (2024) 835–851, https://doi.org/10.1007/s00170-024-13437-7.
[42] R.K. Enneti, S.J. Park, R.M. German, S.V. Atre, Review: thermal Debinding process in particulate materials processing, Mater. Manuf. Process. 27 (2012) 103–118, https://doi.org/10.1080/10426914.2011.560233.
[43] J.A. Moore, B.P. Jarding, B.K. Lograsso, I.E. Anderson, Atmosphere control during debinding of powder injection molded parts, J. Mater. Eng. Perform. 4 (1995) 275–282, https://doi.org/10.1007/BF02649064.
[44] N. Lecis, M. Mariani, R. Beltrami, L. Emanuelli, R. Casati, M. Vedani, A. Molinari, Effects of process parameters, debinding and sintering on the microstructure of 316L stainless steel produced by binder jetting, Mater. Sci. Eng. A 828 (2021) 142108, https://doi.org/10.1016/j.msea.2021.142108.
[45] K. Zissel, E. Bernardo Quejido, S. Bhattacharya, P. Forêt, E. Hryha, Key aspects of the Debinding & Sintering Atmosphere for 17-4 PH stainless steel fabricated via binder jetting, in: Euro PM2023 Proc., EPMA, 2023, https://doi.org/10.59499/EP235761118.
[46] F. Yan, W. Xiong, E. Faierson, G.B. Olson, Characterization of nano-scale oxides in austenitic stainless steel processed by powder bed fusion, Scr. Mater. 155 (2018) 104–108, https://doi.org/10.1016/j.scriptamat.2018.06.011.
[47] L.S. Kremnev, V.V. Svishchenko, D.P. Cheprasov, Structure and mechanism of the formation of granular bainite in steel 20Kh2NACh, Met. Sci. Heat Treat. 39 (1997) 367–370, https://doi.org/10.1007/BF02469059.
[48] N. Bernier, L. Bracke, L. Malet, S. Godet, An alternative to the crystallographic reconstruction of austenite in steels, Mater. Charact. 89 (2014) 23–32, https://doi.org/10.1016/j.matchar.2013.12.014.
[49] Z.X. Qiao, Y.C. Liu, L.M. Yu, Z.M. Gao, Formation mechanism of granular bainite in a 30CrNi3MoV steel, J. Alloys Compd. 475 (2009) 560–564, https://doi.org/10.1016/j.jallcom.2008.07.110.
[50] D. De-Castro, A. Eres-Castellanos, J. Vivas, F.G. Caballero, D. San-Martín, C. Capdevila, Morphological and crystallographic features of granular and lath-like bainite in a low carbon microalloyed steel, Mater. Charact. 184 (2022) 111703, https://doi.org/10.1016/j.matchar.2021.111703.
[51] M. Müller, D. Britz, L. Ulrich, T. Staudt, F. Mücklich, Classification of Bainitic structures using textural parameters and machine learning techniques, Metals (Basel). 10 (2020) 630, https://doi.org/10.3390/met10050630.
[52] S. Zhang, S. Romo, R.A. Giorjao, P.B.P. Leao, A.J. Ramirez, EBSD analysis of strain distribution and evolution in ferritic-Pearlitic steel under cyclic deformation at intermediate temperature, Mater. Charact. 193 (2022) 112293, https://doi.org/10.1016/j.matchar.2022.112293.
[53] S. Zajac, V. Schwinn, K.H. Tacke, Characterisation and quantification of complex Bainitic microstructures in high and ultra-high strength Linepipe steels, Mater. Sci. Forum 500–501 (2005) 387–394, https://doi.org/10.4028/www.scientific.net/MSF.500-501.387.
[54] R.M. Jentner, S.P. Tsai, A. Welle, S. Scholl, K. Srivastava, J.P. Best, C. Kirchlechner, G. Dehm, Automated classification of granular bainite and polygonal ferrite by electron backscatter diffraction verified through local structural and mechanical analyses, J. Mater. Res. 38 (2023) 4177–4191, https://doi.org/10.1557/s43578-023-01113-7.
[55] F. Yang, A. Saxena, L. Riester, Use of the nanoindentation technique for studying microstructure/crack interactions in the fatigue of 4340 steel, Metall. Mater. Trans. A 29 (1998) 3029–3036, https://doi.org/10.1007/s11661-998-0210-2.
[56] L. Liu, B.B. He, G.J. Cheng, H.W. Yen, M.X. Huang, Optimum properties of quenching and partitioning steels achieved by balancing fraction and stability of retained austenite, Scr. Mater. 150 (2018) 1–6, https://doi.org/10.1016/j.scriptamat.2018.02.035.
[57] C.B. Finfrock, A.J. Clarke, G.A. Thomas, K.D. Clarke, Austenite stability and strain hardening in C-Mn-Si quenching and partitioning steels, Metall. Mater. Trans. A Phys. Metall. Mater. Sci. 51 (2020) 2025–2034, https://doi.org/10.1007/s11661-020-05666-8.
[58] S. Lian Chen, Z. Xi Cao, C. Wang, C. Xiang Huang, D. Ponge, W. Quan Cao, Effect of volume fraction and mechanical stability of austenite on ductility of medium Mn steel, J. Iron Steel Res. Int. 26 (2019) 1209–1218, https://doi.org/10.1007/s42243-019-00267-1.
[59] J. Hidalgo, K.O. Findley, M.J. Santofimia, Thermal and mechanical stability of retained austenite surrounded by martensite with different degrees of tempering, Mater. Sci. Eng. A 690 (2017) 337–347, https://doi.org/10.1016/j.msea.2017.03.017.
[60] A. Navarro-López, J. Hidalgo, J. Sietsma, M.J. Santofimia, Influence of the prior athermal martensite on the mechanical response of advanced bainitic steel, Mater. Sci. Eng. A 735 (2018) 343–353, https://doi.org/10.1016/j.msea.2018.08.047.
[61] S. Kumar, S.B. Singh, Quenching and partitioning (Q&P) steel: alloy design, phase transformation and evolution of microstructure, Metall. Mater. Trans. A Phys. Metall. Mater. Sci. 54 (2023) 3134–3156, https://doi.org/10.1007/s11661-023-07085-x.
[62] A. Sierra-Soraluce, G. Li, M.J. Santofimia, J.M. Molina-Aldareguia, A. Smith, M. Muratori, I. Sabirov, Effect of microstructure on tensile properties of quenched and partitioned martensitic stainless steels, Mater. Sci. Eng. A 864 (2023) 144540, https://doi.org/10.1016/j.msea.2022.144540.
[63] L.A. Pinto, D. Pérez Escobar, O.S.H. Santos, N.I.A. Lopes, J.R.G. Carneiro, R. Ribeiro-Andrade, Influence of surface preparation method on retained austenite quantification, Mater. Today Commun. 24 (2020) 101226, https://doi.org/10.1016/j.mtcomm.2020.101226.
[64] I. De Diego-Calderón, M.J. Santofimia, J.M. Molina-Aldareguia, M.A. Monclús, I. Sabirov, Deformation behavior of a high strength multiphase steel at macro- and micro-scales, Mater. Sci. Eng. A 611 (2014) 201–211, https://doi.org/10.1016/j.msea.2014.05.068.
[65] J. Radhakrishnan, P. Kumar, S.S. Gan, A. Bryl, J. McKinnell, U. Ramamurty, Microstructure and tensile properties of binder jet printed 17–4 precipitation hardened martensitic stainless steel, Mater. Sci. Eng. A 860 (2022) 144270, https://doi.org/10.1016/j.msea.2022.144270.
[66] S. Mirzababaei, B.K. Paul, S. Pasebani, Microstructure-property relationship in binder jet produced and vacuum sintered 316 L, Addit. Manuf. 53 (2022) 102720, https://doi.org/10.1016/j.addma.2022.102720.
[67] M. Jamalkhani, M. Asherloo, O. Gurlekce, I.-T. Ho, M. Heim, D. Nelson, A. Mostafaei, Deciphering microstructure-defect-property relationships of vacuum-sintered binder jetted fine 316 L austenitic stainless steel powder, Addit. Manuf. 59 (2022) 103133, https://doi.org/10.1016/j.addma.2022.103133.
[68] Y. Kitahara, S. Takahashi, T. Fujii, Thermal analysis of polyethylene glycol: evolved gas analysis with ion attachment mass spectrometry, Chemosphere 88 (2012) 663–669, https://doi.org/10.1016/j.chemosphere.2012.03.054.
[69] S. Masia, P.D. Calvert, W.E. Rhine, H.K. Bowen, Effect of oxides on binder burnout during ceramics processing, J. Mater. Sci. 24 (1989) 1907–1912, https://doi.org/10.1007/BF02385397.
[70] A.A. El-Geassy, M.I. Nasr, Influence of original structure on the kinetics and mechanisms of carbon monoxide reduction of hematite compacts, ISIJ Int. 30 (6) (1990) 417–425, https://doi.org/10.2355/isijinternational.30.417.
[71] A.A. El-Geassy, K.S.A. Halim, M. Bahgat, E.A. Mousa, E.E. El-Shereafy, A.A. El-Tawil, Carbothermic reduction of Fe 2 O 3 /C compacts: comparative approach to kinetics and mechanism, Ironmak. Steelmak. 40 (2013) 534–544, https://doi.org/10.1179/1743281212Y.0000000076.

[72] X. Duan, H. Yu, J. Lu, Z. Huang, Temperature dependence and formation mechanism of surface decarburization behavior in 35CrMo steel, Steel Res. Int. 90 (2019), https://doi.org/10.1002/srin.201900188.
[73] M. Mariani, D. Mariani, G. Pietro De Gaudenzi, N. Lecis, Effect of printing parameters on sintered WC-co components by binder jetting, Eur. J. Mater. 2 (2022) 365–380, https://doi.org/10.1080/26889277.2022.2076617.
[74] J. Radhakrishnan, P. Kumar, S.S. Gan, A. Bryl, J. McKinnell, U. Ramamurty, Fatigue resistance of the binder jet printed 17-4 precipitation hardened martensitic stainless steel, Mater. Sci. Eng. A 865 (2023) 144451, https://doi.org/10.1016/j.msea.2022.144451.